Characterization and First Results of an Inverse Photoemission Spectrometer

by

Michael Bouliane

A thesis
presented to the University of Waterloo
in fulfillment of the
thesis requirement for the degree of
Master of Science
in
Physics

Waterloo, Ontario, Canada, 2024

© Michael Bouliane 2024

Author's Declaration

I hereby declare that I am the sole author of this thesis. This is a true copy of the thesis, including any required final revisions, as accepted by my examiners.

I understand that my thesis may be made electronically available to the public.

Abstract

This thesis discusses our efforts to characterize our home built inverse photoemission spectrometer. We review the relevant theoretical and practical considerations for the technique of inverse photoemssion spectroscopy. We then detail our efforts to characterize our low energy electron gun, presenting a method for determining the total current delivered by the beam using just a Faraday cup. Measurements of the beam's profile are presented and are used to calculate the parallel momentum resolution of the beam. Equally important is the characterization of our photon detectors, which we show are operating in the proportional region with a minimal dark count rate. We ascertained a spectrometer energy resolution of 415(55) meV by performing inverse photoemission measurements on polycrystalline gold foil, single crystal Cu (111), and pyrolytic graphite. As a final demonstration of our spectrometer's capabilities we provide a full unoccupied band mapping for pyrolytic graphite showing its ability to resolve dispersive electronic features in reciprocal space.

Acknowledgements

I would like to start by thanking Prof. David Hawthorn, my supervisor and mentor. I started in his group as an undergraduate with minimal research experience, and through his guidance I've grown into a confident and capable experimenter. I'm greatly looking forward to continuing on this project with him.

My fellow group members both past and current deserve a great deal of credit as well. Dr. Christopher McMahon for being the one to train me on our instrument and lab protocols years ago, Yuxuan Qi for pushing this project to its conclusion with me, and Rantong Gong and Naman Gupta who are always there to listen and empathize when things invariably go wrong in the lab. I'd also like to thank my fellow graduate students in the office, for providing great conversation over a much needed coffee break.

Thank you to my loving partner Indira, my family, and my friends. Your encouragement makes the hard days easier. And thank you for indulging me and my Niagara Glen addiction, there's no better way to clear my mind than climbing Ontario limestone.

Finally I'd like to thank my examining committee, Dr. Robert Hill and Dr. Adam Wei Tsen, and anyone else reading this work. It covers two years of my life pursuing physics, a dream come true. Thank you for taking the time to read this. I hope you find it insightful and for any new IPES experimenters reading this, I hope I provided a solid foundation for you to build on.

Dedication

This thesis is dedicated to those who choose every day to love me and raise me up. Thank you.

Table of Contents

Author's Declaration ii

Abstract iii

Acknowledgements iv

Dedication v

List of Figures viii

1 Introduction 1

1.1 Overview of Angle Resolved Photoemssion Spectroscopy 2

1.2 Simple Band Example: Bulk Bands and Surface States on Metals 3

1.3 Strongly Correlated Materials: Cuprate Superconductors 6

2 Theoretical and Practical Considerations of IPES 9

2.1 Inverse Photoemission Process 9

2.2 Momentum Resolved IPES 11

2.3 A Note on Detecting Methods 12

2.4 Kinetic Energy and Contact potential 13

2.5 Determining Fermi Energy 14

2.6 Experimental Considerations 15

2.6.1 Vacuum Requirements 15

2.6.2 Sample Preparation Procedures 15

2.6.3 Electron Diffraction 17

3 Electron Source **18**

3.1 Total Beam Current . . . 19

3.1.1 The Need for Quantifying Beam Current . . . 19

3.1.2 Measuring Beam Current . . . 19

3.1.3 Wiener Deconvolution . . . 21

3.2 Beam Divergence and Momentum Resolution . . . 27

3.2.1 Beam Spot Relative to Sample Size . . . 31

4 Photodetectors **34**

4.1 GM Tube Operation . . . 35

4.1.1 Gas Multiplication and Operating Regions . . . 35

4.1.2 Achieving UV Energy Sensitivity . . . 38

4.1.3 Signal Processing . . . 40

4.2 Detector Characterization . . . 42

4.2.1 Operating Mode . . . 42

5 Spectrometer Energy Resolution **46**

5.1 Fermi Edge of Metals . . . 47

5.2 Image Potential States . . . 52

6 Inverse Photoemssion Study of Highly Oriented Pyrolytic Graphite **55**

7 Conclusion **61**

7.1 Future Work . . . 61

References **63**

List of Figures

1.1 1D NFE band dispersion 4
1.2 Shockley state dispersion from Cu (111) ARPES data 5
1.3 Schematic diagram of cuprate DoS 6
1.4 Calculated band structure for optimally doped Bi2212 7

2.1 3D Diagram of IPE Process and Setup 10
2.2 IPES Energy Level Diagram 11

3.1 Difference in electron transmission between Copper and HOPG 20
3.2 Measured radial beam profile and diagram of measurement procedure . . . 21
3.3 Components required for Weiner deconvolution procedure and resulting deconvolved current distribution 24
3.4 Total beam current produced as a function of electron energy 26
3.5 Hidden asymmetry revealed in 5 eV beam profile after deconvolution 27
3.6 Diagram outlining the differences in beam intensity at different distances along its axis 29
3.7 Experimentally measured beam profile and calculated widths 30
3.8 Samples mounted on graphite coated sample plugs 32
3.9 IPE spectrum produced by the graphite background 33

4.1 Cross-section of GM tube 35
4.2 Different operating regions of GM detectors 37
4.3 GM Tube Response Function 39

4.4 Signal processing block diagram 41
4.5 Experimentally determined pulse height distributions of GM detectors . . . 45

5.1 Normal incidence IPE spectrum of polycrystalline gold 49
5.2 Prepared Cu(111) sample and LEED pattern 50
5.3 Normal incidence IPE spectrum of Cu(111) 51
5.4 Prepared HOPG sample and LEED pattern 53
5.5 IPE spectrum showing IP state of HOPG 54

6.1 ARIPE spectrum of HOPG 56
6.2 Dispersion of HOPG IP state 58
6.3 Contact potential determination for HOPG 59
6.4 HOPG E-k map 60

Chapter 1

Introduction

In condensed matter physics the electronic structure of a material is vital in explaining many of its physics properties. The allowed energy levels in solids differ from that of atoms and molecules in that they take on a continuum of allowed values that depend on the momentum of the electron within the material. These are known as energy bands and their momentum dependence is described in what's known as a band dispersion. Like atomic energy levels, these bands can be either occupied or unoccupied and the interactions between these occupied and unoccupied bands can give rise to a plethora of properties.

Metals for example, are able to conduct electricity with little resistance due to the fact that its highest occupied band is only partially full and thus extra electrons can be added to the system at very little energy cost. Band insulators however, have their highest energy occupied band completely filled meaning extra electrons added to the system have to start filling a completely empty band at a higher energy. This extra energy cost means more work has to be done in order for the material to conduct electrons. The energy difference between these two bands in an insulator may vary, or disperse, as a function of electron momentum meaning that some transitions between these bands will be less energetically taxing than others. This concept is important for semiconductors as it determines if a band gap (the smallest energy difference between the highest occupied band and lowest unoccupied band) is direct or indirect. Only semiconductors with a direct band gap can emit photons from transitions between these bands and thus are fit to be used as LEDs. Thus when engineering a semiconductor that one wishes to use as an LED its electronic structure must be experimentally determined to verify if it has a direct band gap.

The technique which is most commonly employed to measure electronic structure is known as angle resolved photoemission spectroscopy (ARPES). This technique takes advantage of the photoelectric effect, using photons, usually in the UV or x-ray range, to excite and remove electrons from a sample which are collected in an energy analyzer [1, 2]. By varying the angle of the sample relative to the detector an experimenter is able to

change the momentum of the collected electrons. Combining the known electron energy and its momentum allows one to deduce the dispersion of the energy bands of a material and thus elucidate its electronic structure. A caveat to this technique is that since it relies on exciting electrons from the material, only bands which contain electrons are able to be probed. In other words, ARPES only has access to the occupied states of a material. Some techniques exist which allows for ARPES to probe unoccupied states, such as pump-probe ARPES, but this has its limits and complications. To fully map the electronic structure of a material, we need a technique which is capable of resolving the unoccupied states and their dispersions. That technique is known as inverse photoemission spectroscopy (IPES), and it is the much less adopted conjugate technique to ARPES[2, 3].

Briefly, IPES is a spectroscopic method which probes the unoccupied electronic structure of materials using low energy electrons. If the energy of these electrons matches that of an unoccupied state in the sample they can couple to it. The electron decays to a lower energy unoccupied state and in doing so releases a UV photon which can be detected by the spectrometer. The emitted photon intensity is then used to quantify if an unoccupied state has been coupled to. In subsequent chapters we will examine the energetics and mechanism of IPES in more detail.

1.1 Overview of Angle Resolved Photoemssion Spectroscopy

To fully understand the need for IPES, it is good to start with a basic understanding ARPES. ARPES is a photon in-electron out spectroscopic method that uses a monochromatic beam of photons to excite and remove electrons from a sample using the photoelectric effect. The minimum photon energy, $\hbar\omega_{\min}$ required to excite an electron from a sample is given by [2]:

$$\hbar\omega_{\min} = \phi_s + E_b \tag{1.1}$$

Where ϕ_s is the work function of the sample and E_b is the electron's binding energy. If the photon energy, $\hbar\omega$, is increased beyond this minimum value then the electron absorbs the energy difference as kinetic energy according to [2] :

$$E_k = \hbar\omega - \phi_s - E_b \tag{1.2}$$

Therefore one can measure the kinetic energy of emitted electrons using a known photon energy and work backwards to determine the binding energy of the state the electron was occupying. This is insufficient if one wants to also determine the momentum of the emitted electrons. To do this, the sample is rotated relative to the detector by an angle θ and the conserved parallel momentum of the electrons, $k_{||}$, is given by [2]:

$$k_{||} = \frac{2m_e E_k}{\hbar} \sin\theta \tag{1.3}$$

Meaning that through varying $\hbar\omega$ and θ, and recording the electron kinetic energy E_k one is able to map the dispersion of the occupied electronic structure.

1.2 Simple Band Example: Bulk Bands and Surface States on Metals

As a concrete example we will examine how ARPES is used to measure the simple dispersion of a surface state on a sample of single crystal Cu (111). Before we can understand surface states however we first need to establish a basic band theory for metals which we can then build upon. The simplest example is that of a 1D monatomic crystal of infinite size using the nearly free electron model, the discussion of which is a condensed version of that found in Ref. [4]. Assume that our crystal extends in the z-direction and that all of the atoms are uniformly spaced with lattice constant a. We can then model the periodic potential created by atoms in the chain using:

$$V(z) = -V_0 + 2V_g \cos\left(\frac{2\pi}{a} z\right) \tag{1.4}$$

We assume that the Fourier coefficient of the potential, V_g, is small compared to the kinetic energy of the electrons. Thus the electrons are not tightly bound to the atoms in the chain, hence the name nearly free electron model. To determine the energy eigenvalues of this system we use Bloch's theorem and solve the 1D Schroedinger equation:

$$\left(-\frac{\hbar^2}{2m_e}\frac{\mathrm{d}^2}{\mathrm{d}z^2} + V(z)\right)\psi(z) = E(k)\psi(z) \tag{1.5}$$

Which results in the following secular equation:

$$[E(k) - (k + 2\pi g/a)^2](E(k) - k^2) = |V_g|^2 \tag{1.6}$$

The energy gap between the two bands is formed by the existence of the periodic potential with magnitude given by $2|V_g|$.

We can bring the sample closer to reality by truncating it past $z = 0$, in essence replacing half of the crystal with vacuum. The potential that models this situation is expressed using:

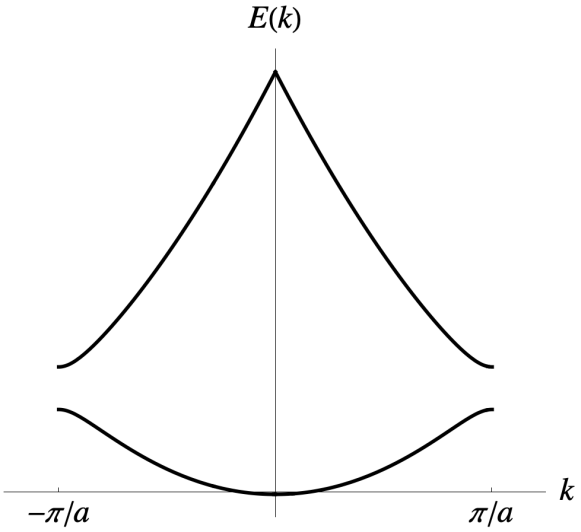


Figure 1.1: 1D Nearly free electron model band dispersion, showing the energy eigenvalues as a function of electron momentum.

$$V(z) = \begin{cases} -V_0 + 2V_g \cos(\frac{2\pi}{a} z) & z < 0 \\ V_1 & z > 0 \end{cases} \tag{1.7}$$

Solving for the wavefunctions of the crystal using this potential we obtain the typical Bloch wavefunctions inside the crystal, and an exponentially decaying wavefunction outside of the crystal. Matching these wavefuntions yields a state which is localized strongly near the surface of the crystal and decays inside of the crystal to match the bulk wavefunctions, and exponentially to zero outside of the crystal. So by simply creating an interface between a crystal described by a periodic potential, and vacuum, we were able to create bound states which localize near the surface of the crystal. For this reason these states are called crystal induced surface states.

ARPES in 3D can be understood through a three-step method whereby an electron is first excited into a bulk final state, from which it then propagates through the sample and is finally transmitted through the surface. The abrupt change in the potential along the z direction as the electron travels from the surface to vacuum leads to the momentum along that direction, denoted $k_\perp$, not being conserved [1]. Conversely, transmission from the surface requires the matching of bulk Bloch states with that of free electron plane waves in vacuum. Due to the translational symmetry imposed by the crystal's surface in the x-y direction, the matching of these states conserves the parallel momentum of the emitted electron, $k_{||}$ [1]. As we will later see, similar arguments are made for parallel momentum conservation in both ARPES and IPES. Since the perpendicular component of momentum

is not conserved, these surface states will disperse only as a function of $k_{||}$, and it can be shown that the dispersion is free electron-like and is given by:

$$E(k_{||}) = E_0 + \frac{\hbar^2 k_{||}^2}{2m^*} \tag{1.8}$$

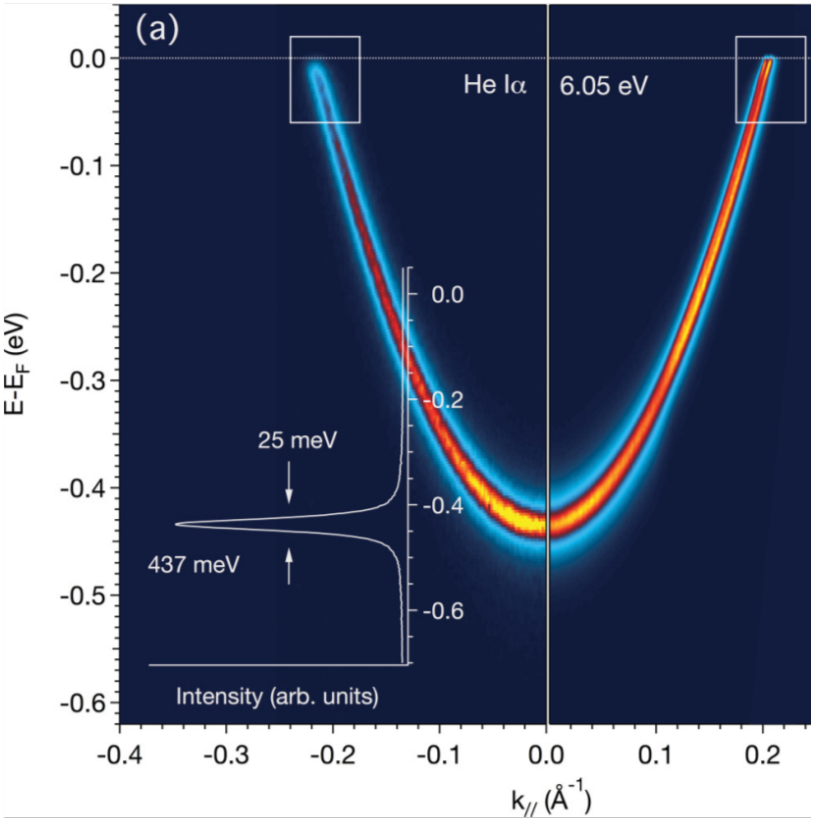


Figure 1.2: ARPES data showing the dispersion of an electronic state in single crystal Cu (111). Cropped from [5], Copyright 2024 by the American Physical Society

This means if we are able to find a material where such states are occupied then we can use ARPES to map the dispersion and should obtain a spectrum that matches with eq. 1.8 very closely. It turns out these states exist in metals, and Fig. 1.2 [5] shows the results of mapping such a state for the (111) crystal face of Copper.

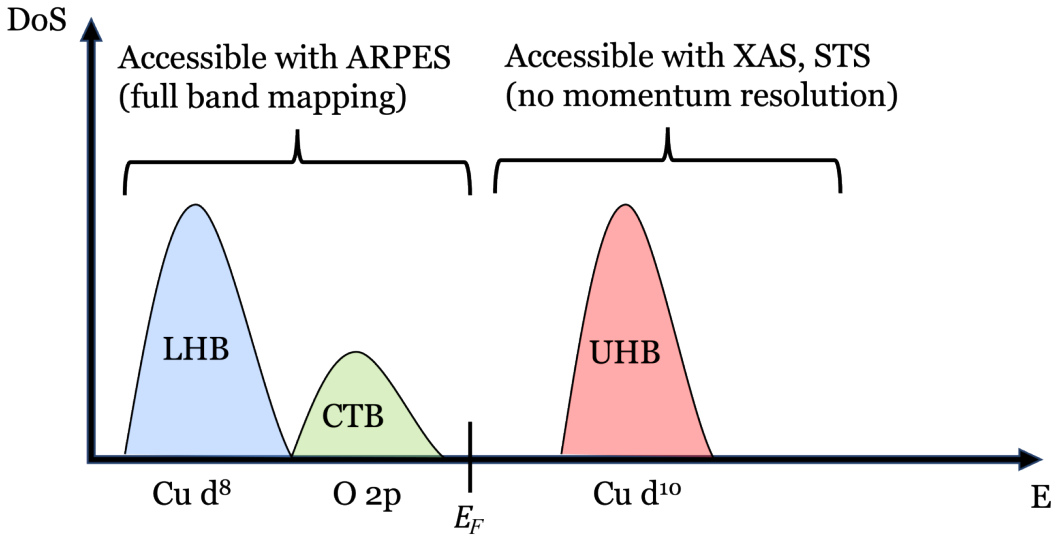


Figure 1.3: Schematic diagram of the densities of states for a typical undoped cuprate, based on the discussion found in Ref. [6] and [7]. States below E_F, the lower Hubbard band (LHB) and so-called in gap states are accessible using ARPES, but the upper Hubbard band (UHB) is completely off-limits unless IPES is used.

1.3 Strongly Correlated Materials: Cuprate Superconductors

The previous section discussed arguably the simplest electronic features which can be theoretically described and experimentally measured. Most materials will have considerably more complicated band structures, and this is arguably most true for the case of strongly correlated materials [6]. In these materials interactions are strong and complex, and fully capturing their behaviour cannot be done using numerical or computational techniques. One of the most famous classes of strongly correlated materials, cuprate superconductors, which our group plans to study extensively using IPES, has an electronic structure which cannot be described exactly and can only be approximated numerically. Experimentally the occupied states have been studied extensively using ARPES [7], but the same cannot be said for their unoccupied states. Doping of these materials is an essential means of tuning their superconducting properties, and we still have very little information on how these unoccupied states disperse as a function of doping [8].

As can be seen in Fig. 1.3, the lower Hubbard band (LHB) and some in gap states, which lie in the charge transfer band (CTB), are fully accessable to ARPES, but the upper Hubbard band (UHB) is inaccessible [7]. A combination of ARPES and IPES would there-

fore allow for the entire electronic structure of these materials to be revealed. Attempts have been made to map these previously inaccessible states, using a pump-probe form of ARPES known as two photon photoemission spectroscopy (2PPE), however only small portions of the Brillouin zone were examined [9]. Alternatively, samples can be doped to change the chemical potential and allow access to portions of the UHB, though it still was not resolved in its entirety [10].

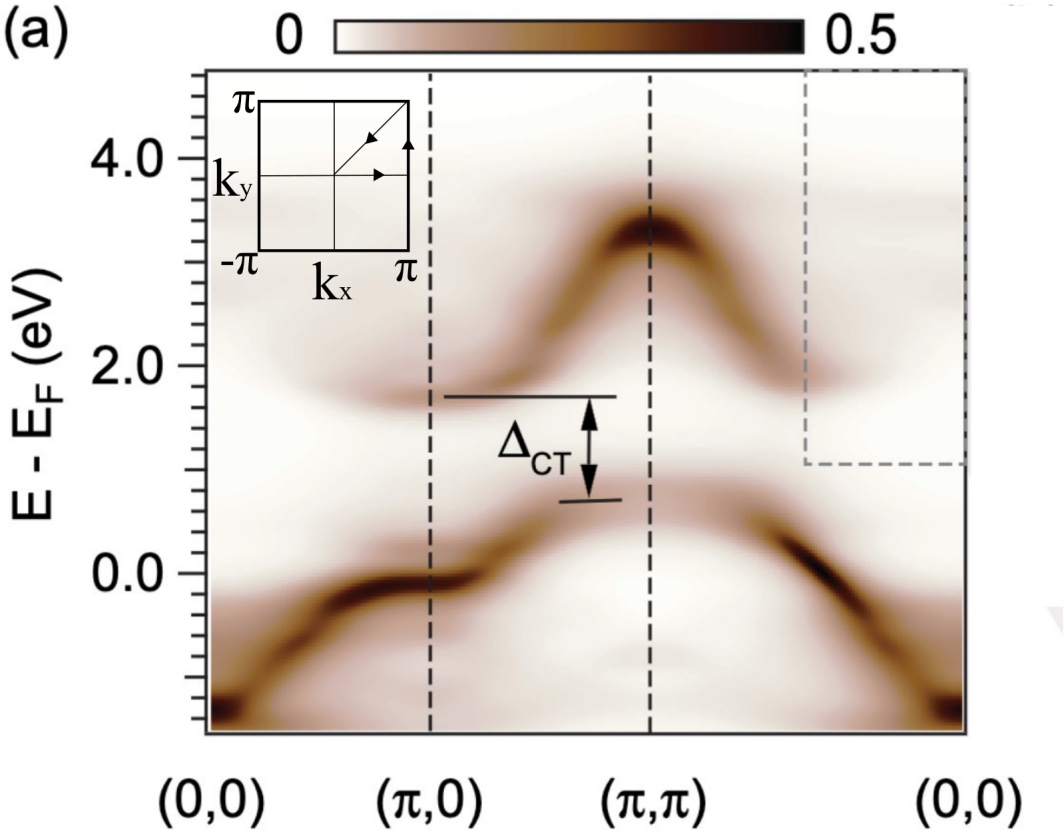


Figure 1.4: Computed band structure for cuprate superconductor Bi2212, obtained using cluster perturbation theory. Grey boxed area indicates the area of reciprocal space which was mapped in the experiment. Inset shows full the full surface Brillouin zone and the arrows represent the path taken to produce the band structure. Reprinted from [9], Copyright 2024 by the American Physical Society.

The grey boxed area represents the area of reciprocal space probed in a 2PPE experiment [9], and as can be seen it leaves the majority of the calculated structure unprobed. IPES grants access to a considerably larger portion of the Brillouin zone (the exact extent

is determined by the sample's lattice constant) and would allow for a much better verification of the calculated electronic structure. There is a wealth of knowledge to be gained by studying the electronic structure of these materials which is essentially untapped, the case for IPES for these sample is obvious.

Due to its niche status there are no commercially available setups for IPES, meaning they must be carefully constructed from scratch by every group wishing to explore the technique. Our spectrometer was developed, designed, and built up by Dr. David Hawthorn and Dr. Christopher McMahon and that process has been detailed in Ref. [11]. Prior to the work of myself and former group member Yuxuan Qi [12], the spectrometer had been dormant for a prolonged time and had not produced any IPE results due to issues with our first iteration of photon detectors developed and designed by our group. The path to get to those first measurements involved a thorough process of characterizing both the electron source and photon detectors. The main subject of my thesis details our work performing these characterization methods, and it is my hope that the experiments detailed in this work will prove useful to both future members of our group and other students delving into IPES.

I begin with a brief introduction to the theoretical aspects of IPES, as well as the practical considerations and techniques which one needs to be aware of. I then describe our efforts to optimize our electron source to achieve a maximal parallel momentum resolution and describe a method to accurately determine the total current delivered by a low energy electron gun using just a faraday cup. I then describe the general operating principles of the gas filled band-pass detectors used in isochromat IPES, and the procedure to explicitly determine the gas multiplication factor of these detectors and thus the corresponding operating mode.

The energy resolution of an IPE spectrometer determines how effectively it can resolve unoccupied states, effectively controlling the uncertainty in an IPES measurement. Quantifying this energy resolution is a vital task for demonstrating the capabilities of a spectrometer, and I outline two experiments which can be used for just that purpose. Finally, I show a series of IPE measurements we performed on pyrolytic graphite which was then used to create a band mapping of its unoccupied states, a full demonstration of our spectrometer's capabilities.

Chapter 2

Theoretical and Practical Considerations of IPES

2.1 Inverse Photoemission Process

At its core inverse photoemission spectroscopy is an electron-in photon-out spectroscopic method. It is the complementary method to the technique of photoemission spectroscopy (PES). IPES is used to explore the structure of unoccupied electronic states which are nominally inaccessible to ARPES. To perform IPES electrons are incident on a sample with their energy tuned such that they couple to an initial unoccupied state. The electron then decays radiatively to a lower unoccupied state. This mechanism is known as inverse photoemission (IPE) and can be thought of as the time reversal of the photoelectric effect [13].

Experimental realization is in principle quite simple. All that is required is a well collimated electron source and a photodetector which is sensitive to the energy of the emitted photons, a schematic of which can be seen in Fig. 2.1. The energetics of IPES are outlined in Fig. 2.2, note that all of these values are referenced to the Fermi energy labeled here as E_F. Initially the emitter cathode of the electron source is grounded meaning that any electrons released from it will have an energy determined solely by the cathode's work function, ϕ_c. The energy of the beam can then be tuned by biasing the cathode relative to ground and expressed by the quantity $E_g = eV_g$. The potential eV_g is varied until its energy matches that of an initial unoccupied state $|i\rangle$ with energy E_i [14, 2].

$$E_g + \phi_c = E_i \tag{2.1}$$

As mentioned above, the electron then decays to an unoccupied state, $|f\rangle$, of lower energy, E_f, and in doing so releases a photon of energy $\hbar\omega$. From this we obtain:

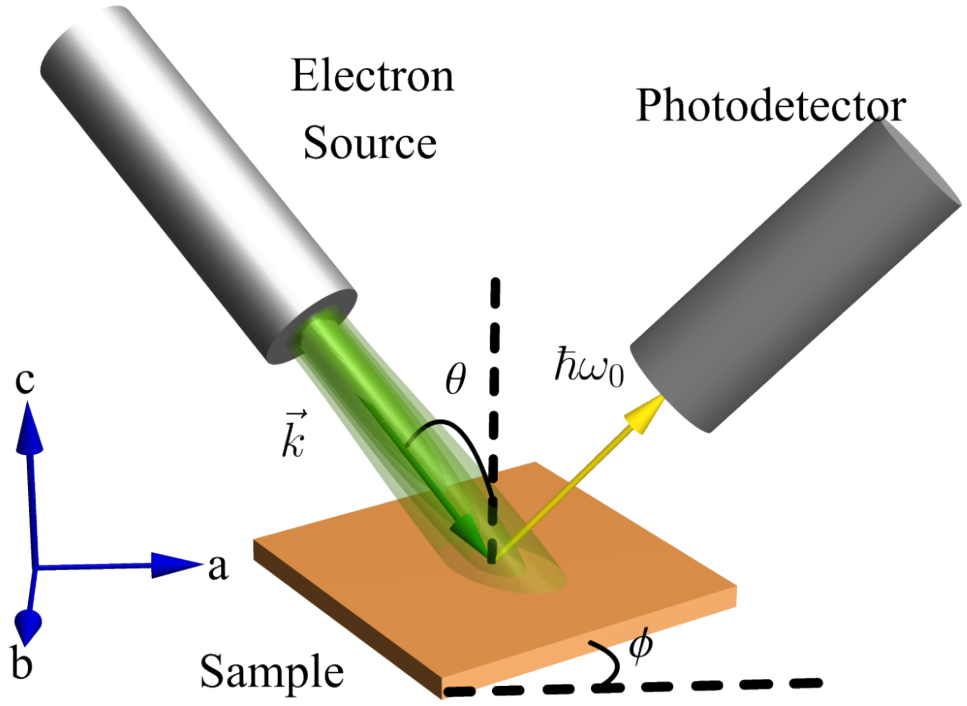


Figure 2.1: Schematic diagram of the inverse photoemssion process and experiment setup. A variable energy electron source is used to send low energy electrons towards the sample. The angle formed between the sample's surface normal, θ, and the electron beam determines the parallel momentum of the electrons and can thus grant access to different states in reciprocal space. Rotation of the sample about its normal (the c-axis in this case) by an angle ϕ can be used to vary the parallel momentum along the in-plane crystallographic axes to fully explore the Brillouin zone.

$$E_f = E_i - \hbar\omega \tag{2.2}$$

Therefore we can combine these two results to determine the energy of the final state in terms of the electron source parameters [15]:

$$E_f = E_g + \phi_c - \hbar\omega \tag{2.3}$$

This is the governing equation for the inverse photoemission process. The goal of an IPE experiment is to vary E_g such that it probes the energies of all unoccupied states, E_f. The data in IPES experiments is presented with energy values relative to the Fermi energy, which is grounded.

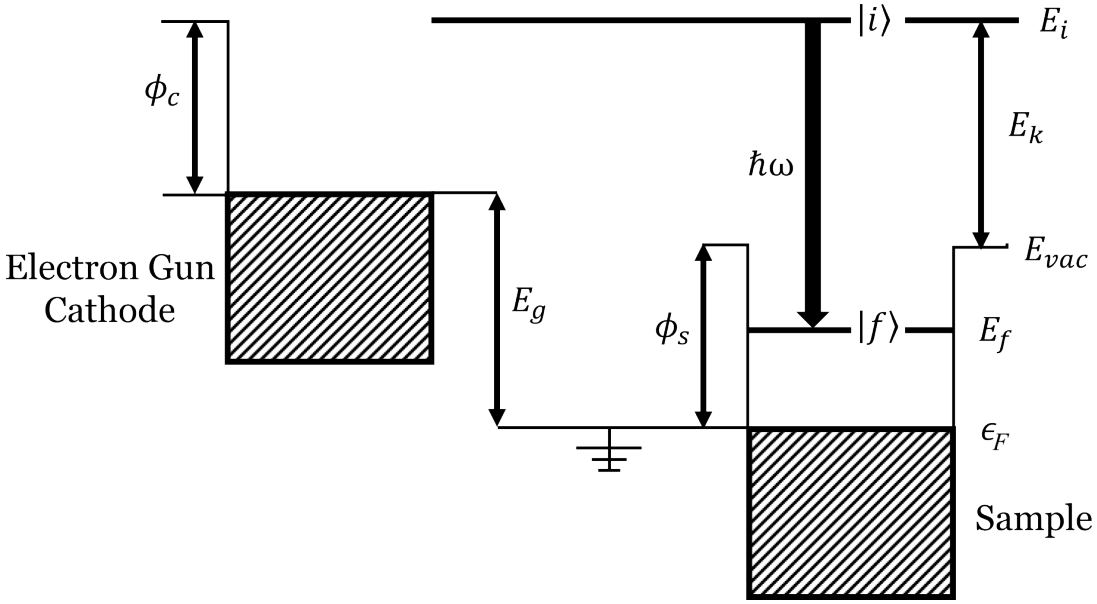


Figure 2.2: Energy level diagram for inverse photoemssion spectroscopy. Electrons are released from a heated cathode and couple to an initial unoccupied state $|i\rangle$. The decay of the electron from state $|i\rangle$ to the lower energy unoccupied state $|f\rangle$ releases a photon which can be collected for detection. For isochromat inverse photoemission spectroscopy band-pass photon detectors are used which fixes the photon energy to a single value, $\hbar\omega_0$. Detections occur only when the energy difference between $|i\rangle$ and $|f\rangle$ is exactly $\hbar\omega_0$.

2.2 Momentum Resolved IPES

Just as PES can be extended to angle resolved PES (ARPES), which allows for the energy of occupied states to be mapped as a function of their crystal momentum by means of varying the angle formed between the sample and detector, angle resolved IPES is also achievable by allowing for the sample to change its orientation relative to the incident electron beam.

Due to the translational symmetry of the sample's surface, the component of the electron's momentum parallel to this, $k_{||}$, is a conserved quantity up to a reciprocal lattice vector [16] as the electron goes from a free electron to one bound in state $|i\rangle$. In the radiative transition to state $|f\rangle$ the electron loses some of its momentum to the released photon. This can cause complications due to needing to know the momentum of the released photon in order to determine the momentum of the final state, which was required in the first iteration of IPE called bremsstrahlung isochromat spectroscopy. This technique used high energy electron beams and detected the released x-rays. This leads to the first experimental consideration I will discuss which is that modern IPE uses low energy electrons (0 eV - 100 eV) so that the released photons are shifted down to the ultraviolet range to energies typically near 10 eV. By doing this the momentum lost to the photon is negligible compared to that of the electron in both state $|i\rangle$ and state $|f\rangle$. This allows one to make the assumption that $k_{||}$ is conserved through the entire IPE process.

In order to quantify the electron's momentum we first need to determine its kinetic energy. This is done by assuming that it is a free electron before it couples to the sample with dispersion given by:

$$E_k = \frac{\hbar^2 k^2}{2m_e} \tag{2.4}$$

From this we can determine the magnitude of the electron's momentum using:

$$k = \frac{\sqrt{2m_e E_k}}{\hbar} \tag{2.5}$$

By defining θ as the angle made between the electron beam and the sample's normal we can express the parallel component of the momentum as [3]:

$$k_{||} = \frac{\sqrt{2m_e E_k}}{\hbar} \sin\theta \tag{2.6}$$

One can then further rotate the sample along its normal by an angle ϕ such that different mirror planes can be explored.

Therefore in an angle resolved IPE experiment we are able to tune the beam energy E_g and sample angles θ and ϕ to couple to unoccupied states as a function of energy and momentum provided one is able to determine the kinetic energy, E_k.

2.3 A Note on Detecting Methods

In Section 2.1 we simply stated that all one needs to perform IPES is a source of electrons and a means of detecting the released photons. While this is true, it is an oversimplification

that I will briefly expand on here. IPE spectrometers are built to operate in one of two ways: spectrograph mode or isochromat mode [3, 15].

In spectrograph mode, a monochromatic beam of electrons is used to irradiate a sample, and all of the photons released are detected. The locations of unoccupied states are determined using peaks in the intensity of photons at an energy satisfying the condition:

$$\hbar\omega = E_g + \phi_c - E_f \tag{2.7}$$

Alternatively, one can use an electron source with a variable energy and restrict the photon detection energy to a single value of $\hbar\omega_0$. In this operating mode we only get peaks in photon intensity whenever the energy between the initial and final states differ by exactly $\hbar\omega_0$. A spectrometer that operates in this way is said to be an isochromat spectrometer and is the design we employ in our lab. For that reason I will limit the discussion in this thesis to be solely on isochromat IPES.

Achieving single photon energy sensitivity will be discussed in greater detail in Chapter 4, but briefly it is done by using a Geiger-Můller tube which is modified to create a band-pass detector. A CaF_2 or MgF_2 entrance window tunes the high-pass portion of the band-pass through its optical transmission, and the photoionization yield of the acetone detection gas sets the low-pass [17].

2.4 Kinetic Energy and Contact potential

Referring back to Fig. 2.2, we see that the kinetic energy is given by [2]:

$$E_k = E_i - E_{\text{vac}} \tag{2.8}$$

If we tune our energy reference to the Fermi level, then the vacuum energy, E_{vac}, is simply given by the sample's work function, ϕ_s. Thus the kinetic energy can be expressed as (substituting in the expression for E_i derived previously):

$$E_k = E_g + \phi_c - \phi_s \tag{2.9}$$

The issue with this equation is that in general, one does not know the exact values for either the cathode work function nor the sample work function. This is solved by introducing the contact (sometimes called Volta) potential, Δ, which is defined as [18]:

$$\Delta = \phi_s - \phi_c \tag{2.10}$$

The work function of the cathode is engineered to be as low as possible so that electrons be more easily removed from it through a process like thermionic emission, which is discussed in Chapter 3.1.3. Thus Δ is always a positive quantity for the sake of IPE and is typically just a few eV in magnitude. The contact potential is a useful quantity due to the fact that when two materials that freely conduct electrons are placed in electrical contact, electrons will flow between the two until their Fermi levels have equalized [19]. Despite the equal Fermi levels of the sample and cathode, due to the difference in work functions between the two an electric potential still exists and represents an energy barrier which the electrons from the cathode must overcome in order to couple to the sample. To accomplish this the cathode needs to be biased with a potential of at least [18]:

$$V_g = \frac{\phi_s - \phi_g}{e} = \frac{\Delta}{e} \tag{2.11}$$

before electrons will couple to the sample and thus transmit current through it. Alternatively, one can choose an arbitrary bias voltage for the cathode and then vary a bias voltage for the sample,V_s, above ground. Current transmission through the sample then occurs when:

$$V_g = V_s + \frac{\Delta}{e} \tag{2.12}$$

Current transmission in such a measurement typically takes the form of a step function allowing for a fitting to be done to extract the value of V_s. Thus the contact potential can be found using [18]:

$$\Delta = e(V_g - V_s) \tag{2.13}$$

With knowledge of the contact potential for a specific sample one is then able to determine the kinetic energy which allows for band mapping. It should be noted that since the contact potential is dependent on the work function of the sample, it varies both between materials and between differing crystal faces of the same material. A worked example of this procedure is shown in Chapter 6.

2.5 Determining Fermi Energy

The Fermi energy is the reference energy used for IPE measurements and determining its value has the same issues present in determining the contact potential, that being we do not know the value of the cathode's work function. To account for this we note that at zero cathode bias the electrons will be unable to couple to an unoccupied state and thus

no photons will be produced. As the bias voltage is increased, so to is the electron energy, until such a point where the electrons have an energy greater than the Fermi energy by exactly $\hbar\omega_0$ [11], i.e.:

$$E_f - \epsilon_f = \hbar\omega_0 \tag{2.14}$$

Therefore we can ascertain the Fermi level of a sample by locating the value of E_g at which photons begin to be emitted. This works to determine the Fermi level if the sample is metallic and thus has unoccupied states at the Fermi level. If instead the sample is an insulator or a semiconductor this procedure will reveal the location of the conduction band minimum. To account for this we use the same technique for determining the contact potential: by placing the sample in electrical contact we can shift its Fermi surface to equilibrate with that of a metallic sample, thus measuring the Fermi level of the metallic sample will reveal the Fermi level of the second sample.

2.6 Experimental Considerations

2.6.1 Vacuum Requirements

Mentioned previously, modern implementations of IPES use low energy electrons in the range of 0 eV to 100 eV. The inelastic mean free path of electrons at this energy is typically just a few Å [20], meaning IPE spectrometers can only probe tens of unit cells or fewer. This makes IPES an incredibly surface sensitive technique and requires a great deal of care in preparing, handling, storing, and measuring samples. Sample need to have a clean and smooth surface to provide the best starting conditions for an IPE measurement; to ensure that the surface remains unblemished all measurements must be conducted under ultrahigh vacuum (UHV) to reduce the buildup of oxide layers and adsorbed gases as much as possible which would otherwise prevent electrons from reaching the sample. Our vacuum system, which uses a combination of turbomolecular pumps backed by dry scroll pumps and a cryopump, is capable of achieving stable pressures well into the range of 10^{-11} torr which a previous group member calculated should provide well over one hundred days of experimentation time [11]. This has since been confirmed by performing measurements with pyrolytic graphite which showed an image potential state that persisted over a month on from first cleaving.

2.6.2 Sample Preparation Procedures

Great care needs to be taken when preparing a sample for IPE measurements, which vary greatly depending on the material properties. Metallic samples, such as Cu (111) or Cu

(100), will typically have built up oxide layers which must be chemically removed. To accomplish this we place the sample in a beaker containing a dilute acidic oxide removing solution. The beaker is then placed in the heated bath of an ultrasonic cleaner. The sample is then dried and cleaned using acetone. Our main method of mounting samples is conductive silver paint [1] which provides a large adhesion strength, temperature resistance, and conductivity. The design of our sample receptacle is outlined in [11], and it allows for in-vacuum azimuthal rotation.

Samples are then transferred to our preparation chamber where we are able to perform Ar^+ bombardment, a process which slowly erodes at the sample's surface a single layer at a time. This is done to expose a fresh surface of the sample in a vacuum environment. The bombardment process is not perfect, and leaves the surface of the sample pockmarked with hills and valleys which must be smoothed before measurements can be taken[21]. This is accomplished through annealing where the sample is heated using a Mo button heater to temperatures of anywhere between 200°C to 500°C, determined by the sample's heating characteristics. This high temperature grants the surface atoms increased mobility and allows for atoms to hop to different sites. Energetically it is favourable for atoms in the hills to migrate and form bonds with their neighbours by filling in the holes left in the surface, since the process of forming bonds costs energy[22]. Thus with sufficient annealing time the sample's surface should rearrange to form one which is smooth on an atomic scale. Once the sample is cooled it is ready for measurements, and examples of this process are demonstrated in Chapter 5.

Layered materials are the second most common material we have used in our lab, and in fact are planned to be the focus of our next main projects. These include pyrolytic graphite (detailed in this work), the topological insulator Bi_2Te_3, and high-T_c cuprate superconductors (especially BSSCO). These materials are all similar in that they share weak inter-layer bonds which makes cleaving them especially easy. One can cleave a single layer of graphite and Bi_2Te_3 for example, using just UHV safe adhesive tape. This means a completely fresh surface can be exposed in pristine UHV conditions without the need for etching or annealing. Other layered materials, including some cuprates, have stronger inter-layer bonds and require methods like post cleaving. With this technique a post is secured to the sample's surface using silver paint, and a sharp force is applied perpendicular to the post. If done correctly the sample should crack along a cleavage plane between the layers leaving a smooth surface. Our linear transfer arm in the preparation chamber ensures that regardless of the cleaving method required, we are able to perform it and produce a clean surface.

[1] SPI Supplies Silver Conductive Paint 05001

2.6.3 Electron Diffraction

Low energy electron diffraction (LEED) is a technique which uses electrons in the range of 50 eV to 200 eV to probe the structure of a sample's surface. We use LEED as a qualitative tool for assessing the quality of our sample's surface and orienting it along high symmetry directions in reciprocal space [23]. The diffraction patterns produced from clean, well ordered single crystal samples should be sharp and reflect the symmetry of the surface Brillouin zone (BZ) of the crystal face being studied [24]. Using the resulting diffraction pattern, we can construct the surface BZ and label the corresponding high symmetry points. The sample can then be rotated azimuthally so that rotations along θ correspond to cuts from the $\bar{\Gamma}$ point to desired high symmetry point.

Chapter 3

Electron Source

The electron source is the heart of an inverse photoemission experiment. For an isochromat spectrometer the source must maintain a collimated beam profile and small spot size over a range of several electronvolts [25]. Normally this would not be an issue, but the requirement of low kinetic energy electrons for VUV IPES, typically in the range of 5 eV to 25 eV in our experiments, makes contradictory requests of the electron source. Due to the many orders of magnitude reduced photon yield of IPE compared to the electron yield of PE, we seek to maximize the flux (i.e current) of electrons reaching the sample's surface. This is caused by the small cross section of the photon production process [13, 26]. Low energy, high brightness beams are however vulnerable to the space charge effect which fundamentally limits the current leaving the source and greatly affects the distribution of the beam itself. Additionally, since low energy electron sources for use in IPES are typically themionic emission type, the cathode temperature plays a significant role in the achievable current [27]. A low cathode temperature prolongs source lifetime, but currents are typically small and less stable due to the increased impact of thermal fluctuations. Higher temperatures will maximize current but run the risk of degrading the cathode material much quicker due to evaporation and chemical reactions at the heated surface.

It becomes immediately apparent that once must carefully tune their electron source such that the resultant beam has a strong emission, which is minimally affected by the space charge effect, and cathode degradation. Thanks to advances in surface science, meeting these requirements no longer requires a group eager to undertake IPE to home-build their electron sources, and numerous commercial solutions are available. This shifts the burden entirely to the optimization and characterization of the source, where the goal is exploring parameter space in order to find a configuration suitable for IPE.

3.1 Total Beam Current

3.1.1 The Need for Quantifying Beam Current

Arguably the most important factor in determining the count rate of an IPE experiment, it is paramount that one strives to maximize the current delivered to the sample under consideration. Most groups, regardless of source design, report achieving currents on the order of 5 μA [25, 27]which in our experience is easily achievable, typically leads to a beam free of spatial distortion, and provides suitably high count rates when paired with tuned detectors. The current delivered to the sample is not constant, and is in fact a non-trivial function of the electron energy (accelerating potential). It is crucial to quantify the energy dependence of the sample current so one can normalize their spectral data to account for higher or lower count rates from changing sample current. As mentioned there are two main factors which impact the sample current: the space charge effect, and the cathode temperature. A source which is purely space charge limited will have a current profile determined by Child's law [28]:

$$J = \frac{4\varepsilon_0}{9}\sqrt{\frac{2e}{m_e}}\frac{V_g^{3/2}}{d^2} \tag{3.1}$$

Where V_g is the accelerating potential applied to the cathode and d is the distance to the sample. Alternatively if one is using a cathode where the current is limited solely by cathode temperature then the sample current is expressed through Richardson's law [29]:

$$J = AT^2\mathrm{e}^{-\beta\phi_g} \tag{3.2}$$

where A is a material dependent constant, T is the cathode temperature, $\beta = 1/kT$, and ϕ_g is the cathode work function. For most applications, the electron source will be operating between these two limits and thus estimating the energy dependence of the sample current is very difficult, if not impossible.

3.1.2 Measuring Beam Current

Thankfully the sample current for this energy range is easily measurable with picoammeters, specifically in our case the Keithley 6485 and 6487. Despite this, there are subtleties to be aware of when one is attempting to quantify sample current. A common approach is to measure the current transmitted through the sample, which one essentially gets for free since this has the added effect of grounding the sample. For many materials this is perfectly suitable, and while it will not provide an exact measure of the current magnitude

reaching the sample, the difference will simply be an energy independent scaling that does not affect the resulting normalization.

This method will fail for samples for which the transmission has a non-trivial energy dependence. Electron scattering (both elastic and inelastic) as well as reflections from the sample's surface causes a reduction in the current transmitted through the sample, and the extent of this can vary as a function of energy. This can be seen very apparently in the low energy electron transmission (LEET) data for pyrolytic graphite, which we have found to be an excellent test sample for characterizing an IPE spectrometer, shown in Fig. 3.1. As an aside, this energy dependence is taken advantage of in a technique known as LEET, which an IPES experimenter gets for free by simply recording the current transmitted through the sample over the course of an IPE measurement, and can provide more insight into the electronic structure of the sample [30]. To accurately measure the current reaching the sample, one must instead employ the use of a Faraday cup.

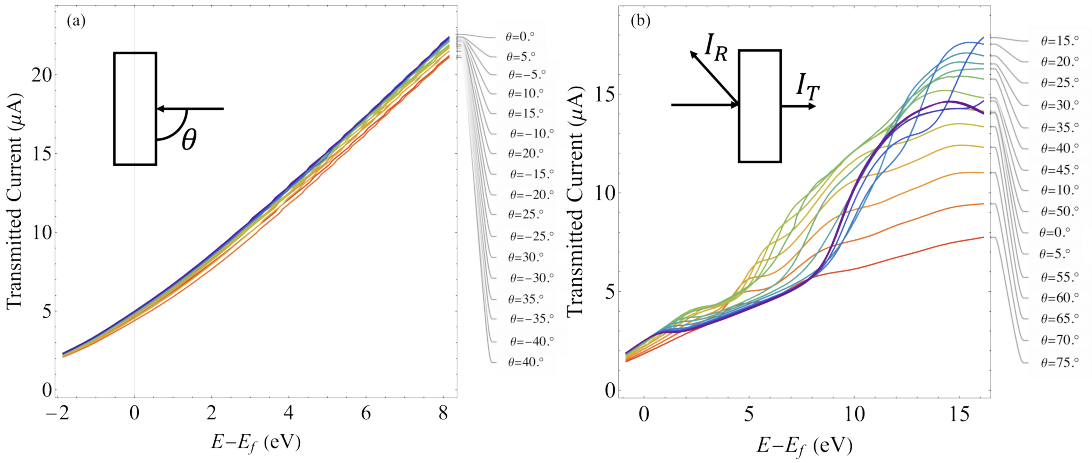


Figure 3.1: Transmitted current magnitude as a function of incident electron energy relative to the Fermi level and sample angle for a) Single crystal Cu (111) and b) Highly oriented pyrolytic graphite. The electronic structure of the copper has little impact on the transmitted current, which is not the case for graphite. The sample dependent transmission shows why transmission current normalization is not a suitable procedure and why we need to perform this deconvolution procedure to determine the total current delivered by the beam agnostic of the sample.

A Faraday cup is simply a metallic cylinder with an often, though not always, circular aperture which is then placed in the path of the beam and measures the resulting current. Crucial to its design is the fact that scattered and reflected electrons are significantly more likely to be captured by the walls of the collector which gives a much closer estimate of the flux entering the aperture. The aperture of our Faraday cup is 1 mm in diameter

meaning that it cannot capture the entire beam profile, which is on the order of two or three millimetres, regardless of how it is positioned. To account for this we raster the Faraday cup in the $x - z$ plane, which in our coordinate system is perpendicular to the beam's axis, and measure the corresponding current. This has the added bonus of measuring the beam's radial profile meaning that we can determine both the total current of the beam and measure the radial symmetry of the beam. This measurement corresponds essentially to performing a convolution of a 1 mm circle function with the actual current distribution of the beam in space; implying that in order to accurately interpret the results of these measurements we must deconvolve the effects of the aperture.

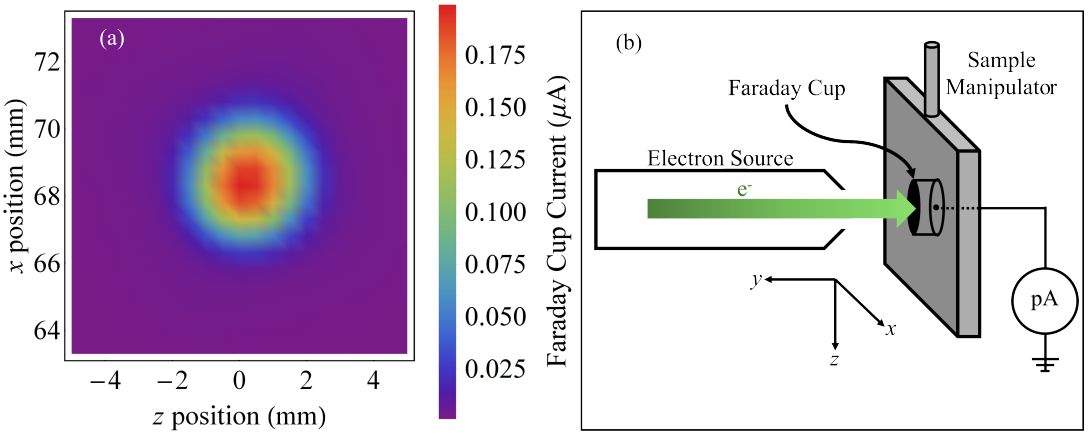


Figure 3.2: a) Example of the radial beam profile which can be measured using the Faraday cup by scanning in the x and z directions. b) Schematic showing how a Faraday cup is used to obtain the profile in a) showing the coordinate axes used for our specific vacuum system.

3.1.3 Wiener Deconvolution

There are many deconvolution procedures which can be followed to obtain the true current distribution, but the one outlined by Sosolik et al. in Ref [31] has been used by other groups specifically for determining the total current of ion and electron beams[32]. I will provide an outline of the technique in this section, but the original Sosolik manuscript and the GitHub repository of R. Mattish [33] are the best resources for implementing this method (which is essentially a Wiener deconvolution). Recall that the measurement is a two-dimensional convolution of our underlying current distribution, denoted $j(\mathbf{r})$, and the aperture of the Faraday cup of radius R_0, which is represented by the following "detector function":

$$d(\mathbf{r}) = \begin{cases} 1 & r \leq R_0 \\ 0 & r > R_0 \end{cases} \tag{3.3}$$

Thus the measured signal can be expressed by the following convolution integral:

$$I(\mathbf{r}) = \int d(\mathbf{r} - \mathbf{r}')j(\mathbf{r}')d\mathbf{r}' \tag{3.4}$$

Which, by means of convolution theorem, can be expressed as a multiplication of functions in k-space. Defining $D(\mathbf{k})$ as the transformed detector function, and dividing through by $D(0) = \pi R_0^2$ (i.e. the detector area), we obtain:

$$I_n(\mathbf{k}) = J_n(\mathbf{k})D_n(\mathbf{k}) \tag{3.5}$$

Where n indicates the quantity has been normalized by $D(0)$. This allows us to explicitly determine the Fourier transformed detector function:

$$D_n(\mathbf{k}) = \frac{2J_1(kR_0)}{kR_0} \tag{3.6}$$

where $k = |\mathbf{k}|$ and J_1 is a Bessel function of the first kind with $\nu = 1$. The nature of the detector function is such that high frequency noise can dominate the current signal, so a Wiener optimized filtering procedure is applied to reduce the additive noise in the measurement. A noisy expression for the measured signal is given by: $I(\mathbf{r}) = d(\mathbf{r}) * j(\mathbf{r}) + n(\mathbf{r})$, or in k-space as:

$$I_n(\mathbf{k}) = J_n(\mathbf{k})D_n(\mathbf{k}) + N_n(\mathbf{k}) \tag{3.7}$$

We introduce the Fourier transformed noise-to-current ratio:

$$\eta_n(\mathbf{k}) = \frac{1}{|D(0)|^2} \frac{|N(\mathbf{k})|^2}{|J(\mathbf{k})|^2} \tag{3.8}$$

and can finally express the Fourier transformed current distribution as:

$$J_n(\mathbf{k}) = \frac{I_n(\mathbf{k})D_n(\mathbf{k})^*}{|D_n(\mathbf{k})|^2 + \eta_n(\mathbf{k})} \tag{3.9}$$

Present in equation 3.9 are the quantities $I_n(\mathbf{k})$ and $D_n(\mathbf{k})$ which can be determined through a discrete FT and evaluation of equation 3.6, respectively. The issue lies in evaluating $\eta_n(\mathbf{k})$, however we can use an insight into the form of $D_n(\mathbf{k})$, seen in Fig. 3.3 to

estimate the form of the noise-to-current ratio. We notice that for small $\mathbf{k}$, $D_n(\mathbf{k})$ is close to 1 and thus $I_n(\mathbf{k}) \approx J_n(\mathbf{k})$. Conversely at large $\mathbf{k}$ the Fourier transformed detector function tends to zero and thus $I_n(\mathbf{k}) \approx N_n(\mathbf{k})$. Put simply, for small $\mathbf{k}$ the signal dominates in the measurement, while the noise dominates at large $\mathbf{k}$. To estimate the magnitude of the noise we examine a radially averaged power spectrum of the measured signal, denoted $\langle |I_n(\mathbf{k})|^2 \rangle$, however this will not provide us with the k-dependence.

In order to estimate the k-dependence of $\eta_n(\mathbf{k})$ we evaluate 3.9 assuming that $\eta_n(\mathbf{k}) = \eta_0 = 0.01$ and that $N_n(\mathbf{k})$ is a constant; choosing this value of η_0 minimizes the high frequency noise in $J_n(\mathbf{k})$. Using this estimate we then compute $|J_n(\mathbf{k})|^2$ and normalize the result such that $|J_n(0)|^2 = 1$. This allows us to re-express equation 3.8 as:

$$\eta_n(\mathbf{k}) = \frac{\eta(0)}{|J(\mathbf{k})|^2} \tag{3.10}$$

Where all of the k-dependence is stored in $|J_n(\mathbf{k})|^2$ and the scaling comes from the value of η which is typically of the order 1×10^{-5} to 1×10^{-2}. This can be estimated by performing a power law fit to the large k portion of the radially averaged power spectrum and extrapolating back to $k = 0$, as shown in Fig. 3.3.d .

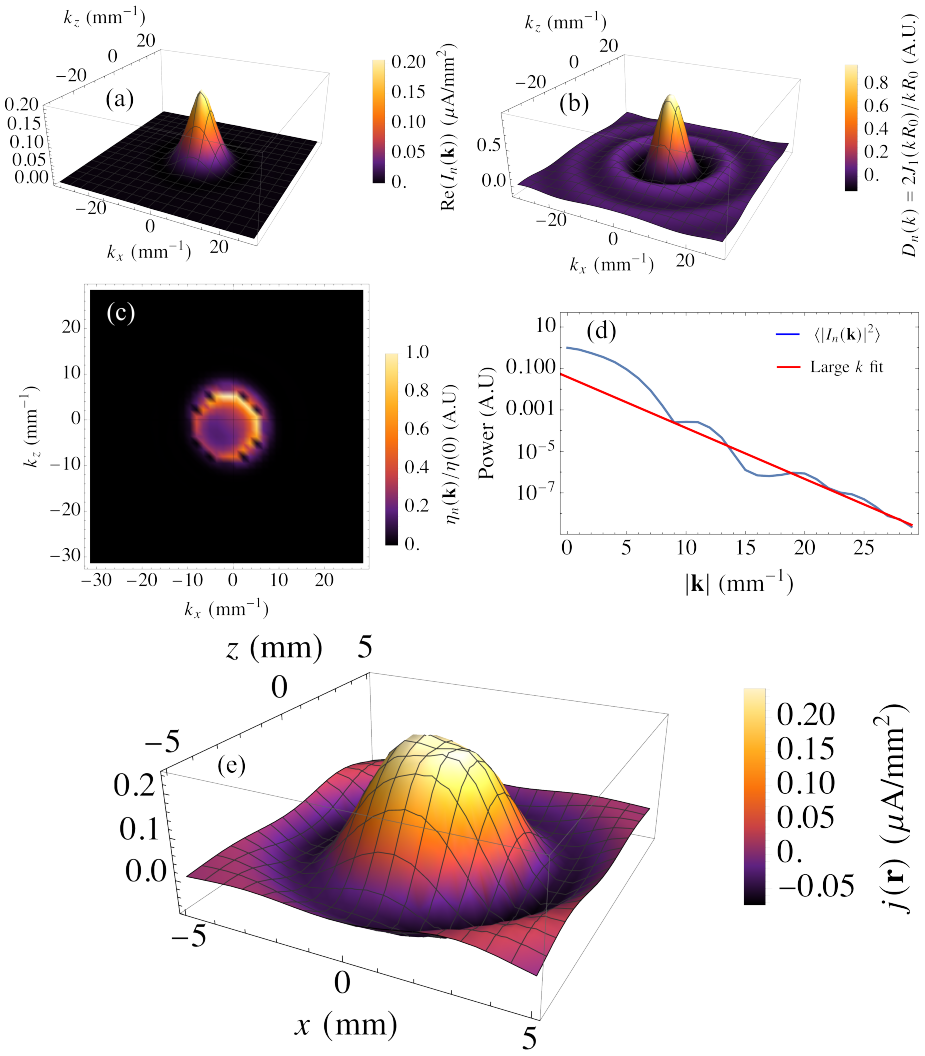


Figure 3.3: a) Fourier transform of measured current profile, $I_n(\mathbf{k})$ b) Fourier transform of the detector function, $D_n(\mathbf{k})$ c) Fourier transformed noise-to-current ratio, $\eta_n(\mathbf{k})/\eta(0)$ d) Radially averaged power spectrum, $\langle|I_n(\mathbf{k})|^2\rangle$, created by integrating $I_n(\mathbf{k})$ over disks of increasingly large radii. A power law fit is performed over the large k values to determine an estimate of the noise at small k values e) Inverse Fourier transform of the current distribution after the deconvolution procedure has been performed. A Gaussian profile can then be fit to this data in order to extract the total current delivered by the beam, I_0. Note that the undulations are artifacts reflecting the fact that a deconvolution of a circular detector function was performed (see Airy disks for a similar phenomenon).

With a full estimate of $\eta_n(\mathbf{k})$ acquired, we then evaluate equation 3.9 a final time, which yields an estimate of the Fourier transform of the current distribution which has been deconvolved from the detector. A final inverse Fourier transform gives an estimate for the current distribution in real space. To this estimate we can perform a Gaussian fitting using:

$$j(x,y) = \frac{I_0}{2\pi\sigma^2} \exp\left(-\frac{(x^2+y^2)}{2\sigma^2}\right) \tag{3.11}$$

Where I_0 is the total current delivered by the beam that we sought to find in the first place. Therefore by applying the described Wiener deconvolution procedure and fitting a Gaussian function to the resulting distribution we are able to accurately estimate the total current delivered by the beam, free from the influence of energy dependent transmission. As an added bonus we also extract the beam's standard deviation which can be used to estimate the true beam width calculated using:

$$\text{FWHM} = 2\sqrt{2\ln 2}\sigma \tag{3.12}$$

Fig. 3.3 shows the results of applying this method to a raster scan of dimensions 10 mm×10 mm for a beam energy of 10 eV. We obtain a noise estimate of $(3.9 \pm 2.8) \times 10^{-2}$, and a resulting Gaussian distribution with a total current of 6.45 ± 0.23 μA. Comparing this with Fig. 3.1 we see that this is slightly larger than the current transmitted through a copper sample at the same kinetic energy, which is what we would expect based on the fact that only a portion of the initial beam current is transmitted through the copper sample.

With a working procedure for estimating the total beam current from Faraday cup data we then varied the kinetic energy and performed the same $x-z$ raster scans, recording the beam current at each position. After then performing the deconvolution procedure and extracting I_0 values we fit an interpolation function which allows us to estimate the total current being delivered to a sample at any energy within this range which is shown in Fig. 3.4.

While a clear trend which in the data can be observed that matches the results of groups who have performed similar analyses for electron sources to be used in IPES, it is apparent that there are large deviations from this trend at certain energies. There are multiple reasons this may be occuring, notably is the fact that the working distance of each measurement remained constant. For an energy setting of 10 eV used in testing, the working distance was close to the beam waist and so the resulting beam spot was well resolved within the 10 mm × 10 mm image. The location of the focal spot, and thus the beam, is energy dependent for constant focusing potentials, meaning that some energy values will be poorly captured in the image which impacts how well the deconvolution and fitting can be performed. Since this procedure will need to be performed any time

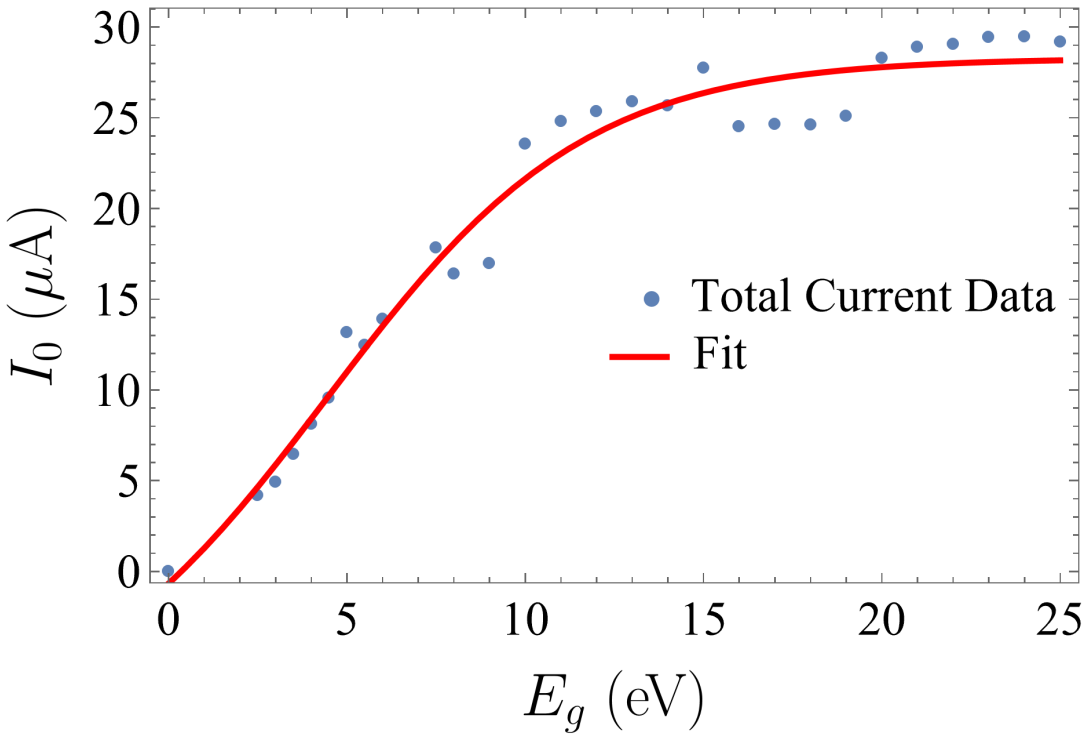


Figure 3.4: Total current delivered by our electron source as a function of electron energy, determined by performing deconvolution and Gaussian fitting. A tanh function was fit to the data to serve as an interpolation function so that we could estimate the total current at any electron energy within this measured range.

the electron source has been reconfigured, we can achieve better results by first scanning the Faraday cup along the path of the beam and determining the focal point location at each energy and performing the raster scan at that location. Ideally the focal point should not drift much over our desired energy range since to maximize our parallel momentum resolution, however in practice it is very difficult to find a suitable configuration which focuses the beam sufficiently at all relevant energy values.

Additionally, this data was taken over the course of several days and with the main chamber cryopump out of service which allows for temperature drifts in the emitter and changes in the vacuum environment over time to impact the resulting beam profiles. Therefore we simply need to perform these measurements at the same relative beam position, in a stable vacuum environment and after having allowed the emitter to reach thermalization.

As an interesting aside, since this deconvolution procedure gives us access to the absolute current density, we are able to easily identify radial asymmetries that would otherwise

be smoothed out in Faraday cup measurements. A notable example of this occurred when we were examining the beam spot at an energy of 5 eV, what first seemed to be a circular profile was revealed to be significantly skewed, desmonstrated in Fig. 3.5.

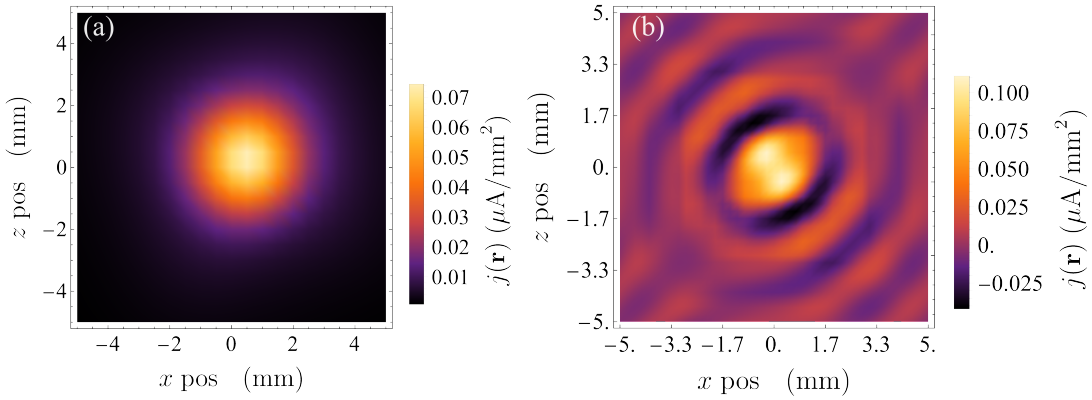


Figure 3.5: a) 5 eV current profile as measured directly with the Faraday cup, which is seemingly perfectly radially symmetrical b) 5 eV profile after performing the deconvolution procedure which reveals a significant asymmetry in the beam that would greatly impact the parallel momentum resolution if not addressed.

Ultimately we have found that when combined with this deconvolution procedure Faraday cup measurements are an excellent way to characterize the performance of low energy electron beams for use in IPES. Additionally, since most groups will be using a Faraday cup for the sake of sample alignment or have a translation stage to which one could easily be mounted, makes this one of the easiest and cheapest ways to accurately probe beams.

3.2 Beam Divergence and Momentum Resolution

A notable feature of IPES, as previously stated, is its ability to resolve the energy dispersion as a function of momentum. If one wishes to study the electronic structure of quantum materials, for example Dirac cones in topological insulators, or the upper Hubbard band in high T_c cuprate superconductors, then it is of the utmost importance to maximize the momentum resolution to ensure these features are fully resolved. In IPES specifically the momentum resolution has a complicated dependence on both the electron kinetic energy and the resulting beam characteristics. In the previous section I mentioned the need for a small spot size and collimated beam and here we examine why. Recall that the parallel component of the electron momentum can be expressed as:

$$k_{||} = \frac{\sqrt{2m_e(E_f + \hbar\omega_0 - \phi_s)}}{\hbar} \sin\theta \tag{3.13}$$

$$k_{||} = \frac{\sqrt{2m_e(E_g - \Delta)}}{\hbar} \sin\theta \tag{3.14}$$

If we neglect the finite energy resolution contribution we find that the associated uncertainty in parallel momentum (i.e. the resolution) is approximated by:

$$\Delta k_{||} = \frac{\sqrt{2m_e(E_g - \Delta)}}{\hbar} \cos\theta \Delta\theta \tag{3.15}$$

The quantity $\Delta\theta$ is known by many names in the literature, but from here on will be called the angular resolution or beam divergence angle. Ref [34] discusses at great detail the ambiguity of momentum and angular resolution in IPES and provides a good discussion on the techniques which can be used to quantify it. As can be seen in equation 3.15 issues arise immediately from the fact that the momentum resolution depends explicitly on the beam's kinetic energy as well as its associated divergence angle. Interestingly we also see that the photon energy $\hbar\omega_0$ affects the momentum resolution, which is the reason isochromat IPES commonly detects photons in the VUV energy range and has shifted away from x-rays. Therefore we see that for increasing kinetic energy we need to counteract its effects by tightening the beam's divergence. Ideally, we would have the beam completely parallel (collimated) and thus divergenceless. To accomplish this we would strive to minimize the beam spot so as to mimic a point source [34]. Realistically this is impossible, so we instead seek to minimize the spot size and then tune to electron optics such that the beam is as close to parallel as possible. Sadly we must also compete with the space charge effect which is also a function of energy and fundamentally limits how tightly the beam can be focused.

When tuned correctly the profiles of low energy electron sources for IPES are typically Gaussian in shape, with a spot size on the order of a few mm. To be precise, it is commonly accepted that the beam spot is defined as the FWHM of the beam at its focal point; the FWHM at a general spot along the beam's axis is referred to generally as the width. The Gaussian nature of the beam makes determining the corresponding angular resolution trivial. If one measures, far from the focal point of the beam, two widths w_i and w_f a distance of ℓ apart, then the beam's divergence is given by:

$$\Delta\theta = 2\arctan\left(\frac{w_f - w_i}{2\ell}\right) \tag{3.16}$$

Ref [34] makes note that in Fig. 3.6, one can potentially misrepresent their angular resolution by measuring at incorrect positions in the beam, for example measuring at

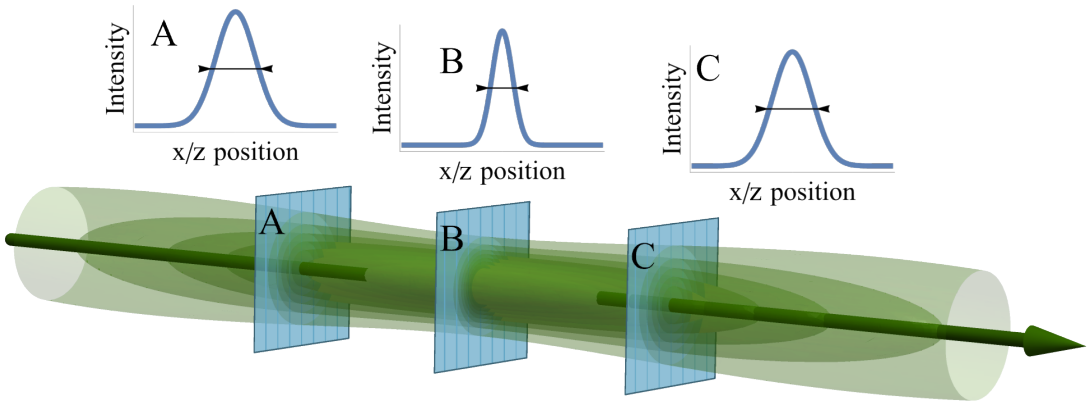


Figure 3.6: A, B, and C are different positions along the beam axis where one could scan a Faraday cup and determine the resulting intensity profile. As is mentioned in [34], if one were to measure at just position A and C where the widths of the intensity profiles are identical, one may conclude falsely that their beam has a much lower divergence angle. To counter this we record the intensity profile over a large extent of the beam so that we can examine how its width varies as a function of working distance and thus more accurately determine our divergence angle.

positions A and C will yield a beam with no apparent divergence, even though the beam is clearly Gaussian along its axis. To account for this, we perform a similar raster scan to the one described in Section 3.1.2 but now in the x-y plane (i.e. parallel to the beams axis). To ensure that we are central along the beam a series of alignment scans are performed with the Faraday cup along the x and z dimensions, until the Faraday cup is located on the centre of the beam spot.

Once the scan is completed we are left with an axial cross section of the beam to which we can perform a fitting and extract the resulting beam widths. By plotting the beam's width as a function of position along the beam, we are able to locate the beam's focal point and can thus evaluate equation 3.16 in the far focus limit, where it is valid.

Fig 3.7 shows the beam intensity as a function of position along (y) and across (x) the beam. To determine the beam width, we group the data according to its y coordinate and fit a Gaussian to the corresponding current intensity and x position data. Unlike in Section 3.1.3 we do not need to perform a two dimensional convolution. Instead, we model the detector as a rectangular function of width 1 mm and fit the result of convolving the detector function with a Gaussian to the data.

Part (b) of Fig. 3.7 shows the extracted FWHM of the beam as a function of position along the beam's axis. We see a clear focal point at a position of $y = 5$ mm, where the spot size is 2.78 mm. From the reports of other groups performing IPES, a spot size on

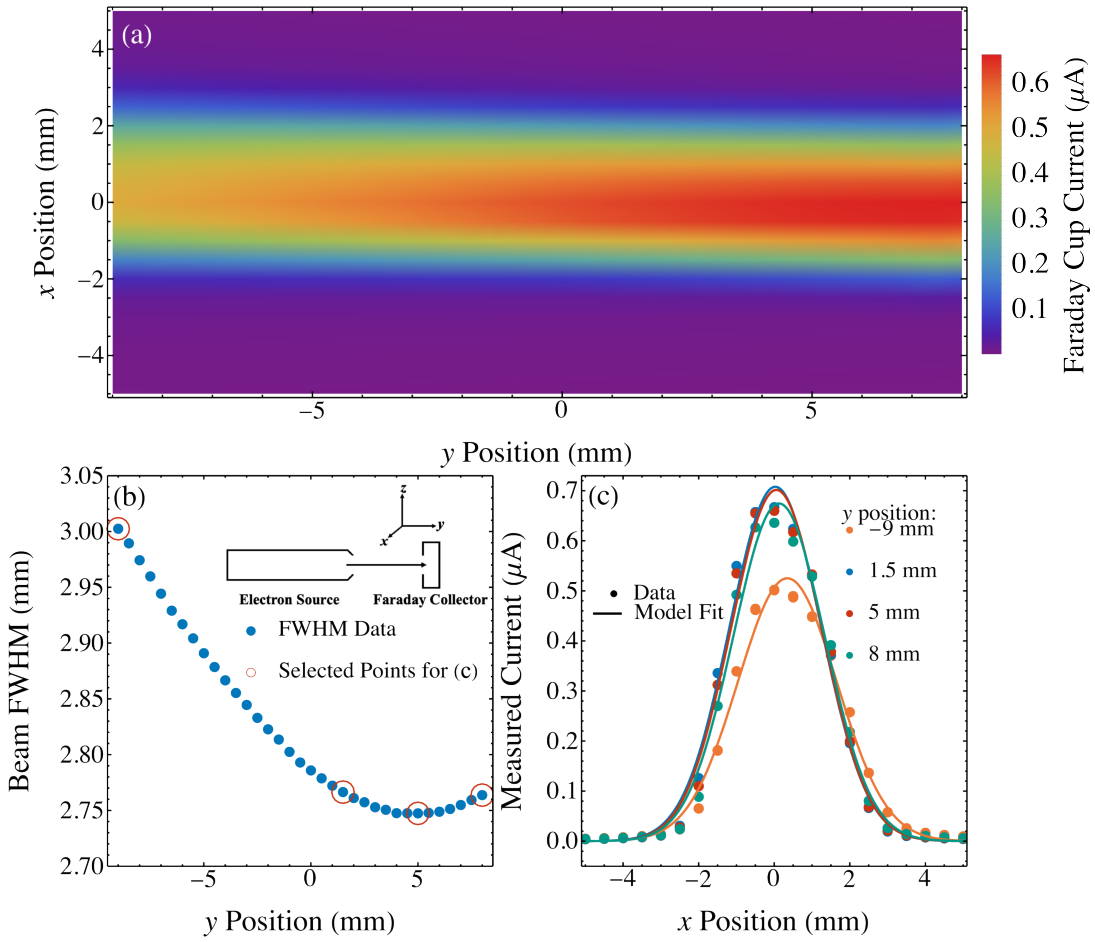


Figure 3.7: a) Beam intensity profile as measured by the Faraday cup as a function of distance across the beam (x position) and distance along the beam axis (y position) b) Beam FWHM as determined by fitting a Gaussian convolved with a 1 mm rectangular function to represent the aperture of the Faraday cup. We selected a few points to examine the quality of fit in panel c) and indicate them using red circles. c) Selected beam intensity profiles at varying locations along the beam axis.

the order of 1 mm - 3 mm is to be expected for these types of sources[27, 25], and is just slightly larger than the minimum achievable spot size as reported by STAIB instruments [35].

Further expanding on the results in Fig. 3.7.b, we are able to evaluate equation 3.16

and obtain an angular resolution of 1.5°, which indicates that in this configuration and at an energy of 10 eV, the beam is very well collimated. To further emphasize this point, we can examine the worst case parallel momentum resolution, which by equation 3.15 occurs at normal incidence (i.e $\theta = 0°$). Inserting our angular resolution and the corresponding kinetic energy we obtain a worst case parallel momentum resolution of just 0.04 $Å^{-1}$, which is not only very closely aligned with the results obtained in Ref [34] who also obtained a parallel momentum resolution of 0.04 $Å^{-1}$ though their experimental method differs greatly from ours so it is unclear how relevant a direct comparison is, but is more than sufficient to accurately map features in the first Brillouin zone.

3.2.1 Beam Spot Relative to Sample Size

For our test samples (Cu and HOPG) with dimensions 10 mm × 10 mm, this spot size is more than sufficient to focus entirely within the sample area. However, we plan to perform IPE measurements on a variety of high T_c cuprate samples which are commonly just a few millimetres in size. Thus a significant portion of the beam will fall outside of the sample, striking the copper sample plug which could contribute a non-trivial background to the underlying signal. To counteract this, we have begun preliminary experiments of coating our sample plug first with an isopropyl alcohol based graphite aerosol. This is UHV compatible, and due to the amorphous nature of the deposited graphite should allow for a smooth background which minimally distorts the desired signal. Two examples of this are shown in Fig. 3.8 for a sample of polycrystalline gold foil and Bi_2Te_3. It is important to check for good electrical contact between the sample and sample plug to ensure that no charging occurs during measurements. Preliminary tests have revealed that the graphite provides a smooth, linearly increasing background which should have minimal effect on genuine spectral features which can be seen in Fig. 3.9.

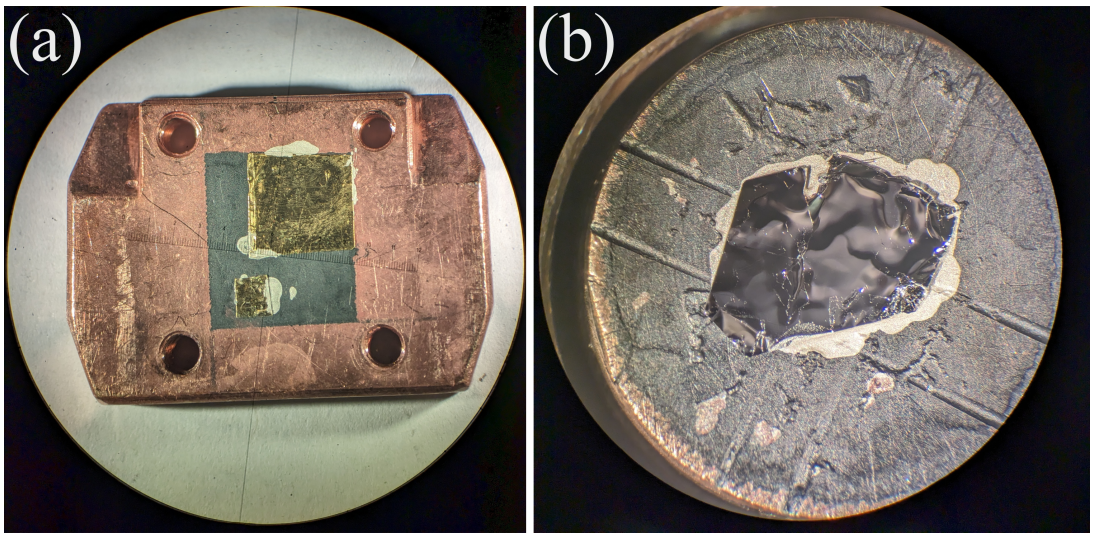


Figure 3.8: Samples of a) polycrystalline gold foil and b) Bi_2Te_3 to provide a smooth background with minimal interference to the sample's spectrum.

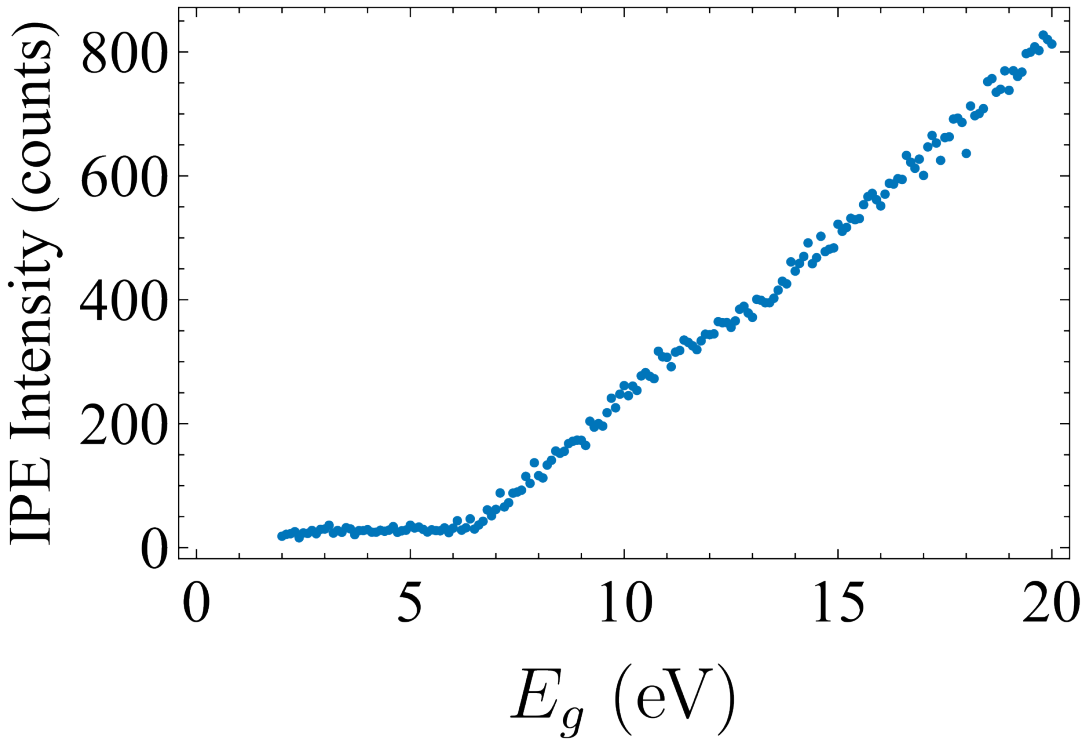


Figure 3.9: Spectrum obtained by performing IPES on the graphite-only region of the sample shown in Fig. 3.8. We observed a smooth, linear increase in IPE intensity once the electron energy passes the Fermi energy.

Chapter 4

Photodetectors

Of equal importance to the electron source are the photodetectors, which allow the spectrometer to observe the emitted UV photons. The type of photodetector used determines the operating mode of the spectrometer [3]: solid state detectors in combination with a diffraction grating are used with monochromatic electron beams in a technique called spectrograph IPES. By rotating the diffraction grating photons of different energies will fall on the detector, allowing one to map the emitted photon intensity as a function of energy. Alternatively, one can use a polychromatic (i.e. variable energy) electron source and limit the observable photon energy to a narrow range around a specific energy value. In essence this an ideally very narrow band pass filter for photon energies, giving this technique the name isochromat inverse photoemission. Most groups, ours included, opt to build isochromat IPE spectrometers where the most common photodetector type are gas filled Geiger-Müller (GM) tubes due to the balance of low cost and large solid detection angle

At their core, GM tubes are general ionizing radiation detectors and have a long history of applications in a variety of fields. For IPES we specifically use end window type GM detectors, where a central anode wire runs through a cylindrical tube that is capped with a material that is transparent to the radiation which is to be detected. The tube is then pressurized with a detecting gas, the purpose of which is to be ionized by incoming radiation. A high voltage bias is applied to the anode wire, this accelerates the liberated electrons and results in further ionizations from the resulting collisions, known as a Townsend avalanche. The electrons make their way to the anode where they are picked up and form a current pulse which can be fed into detector electronics; the ionized gas molecules then drift towards the cathode where they are neutralized and become ready for subsequent detections. It becomes immediately obvious that there is a massive parameter space spanned by the tube pressure, type of detecting gas, tube geometry, entrance window material, and anode voltage. All of which have to be carefully chosen and optimized for

IPES so that the detectors are sensitive only to a specific VUV energy with a maximized quantum efficiency to compensate for the small cross section of the IPE process.

4.1 GM Tube Operation

4.1.1 Gas Multiplication and Operating Regions

In this section I will provide a brief but sufficient explanation of GM tube operation as it pertains to isochromat IPES. G. Knoll's *Radiation Detection and Measurement* [36] provides a very thorough description of all aspects of gas filled ionizing radiation detectors. As mentioned above, GM tubes rely on a high voltage anode to amplify the signal from the ionization of a detection gas; this process is known as gas multiplication. The extent of multiplication, and the mechanism by which it occurs, is a complex function of the tube's configuration.

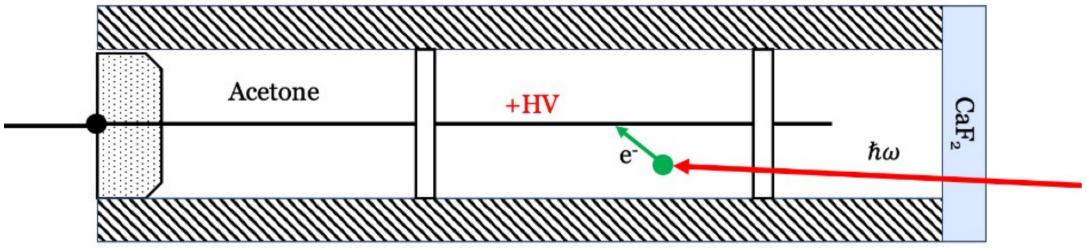


Figure 4.1: Cross-section of an end-window type Geider-Můller tube employed in IPES. Photons enter through a window of either CaF_2 or MgF_2 that provides a lower limit to the allowed photon energy based on their transmission profiles. Photons with energies above the ionization potential of acetone (IP) will ionize a molecule of acetone vapour used to pressurize the tube. If a sufficiently high potential is applied to the central anode wire then the liberated will electron will be accelerated towards it, and with a sufficiently small mean free path will collide with other molecules of acetone. This collision liberates another electron which can be accelerated and cause subsequent ionizations. These so-called Townsend avalanches allow GM tubes to act as photomultipliers, and when made into band-pass detectors make them perfectly suited for the single photon energy senstivity required in isochromat IPES.

The process begins when, for the purposes of IPES, a UV photon with energy $\hbar\omega > IP$ ionizes a molecule of detection gas; the free electron-ionized gas system is called an ion pair. This occurs regardless of anode voltage, and with no voltage applied the free electron will rejoin the ionized gas molecule in a process called recombination. This alone is not sufficient to detect radiation using a GM detector since there is no mechanism by which the

free electrons can reach the anode wire. As the anode voltage is increased the magnitude of the electric field within the tube increases, eventually when the anode voltage is large enough the resulting field magnitude will begin to prevent the recombination of ion pairs. This occurs due to the free electrons being more attracted to the anode wire than the ionized gas molecules and as a result a detectable current is formed through the anode. The kinetic energy of the accelerated electrons at this field strength will be insufficient to cause further ionizations and therefore the collected current is exactly proportional to the charge of the free electrons produced in an ionization event. A tube operating in this mode is said to be acting in the ionization chamber region. Interestingly, due to the lack of multiplication the output current will be a continuous signal, which as we will see is not the case at higher anode voltages.

As the anode voltage is further increased, a second threshold is crossed where the free electrons are of sufficient energy that their collisions with neutral gas molecules can lead to further ionizations. This is the onset of gas multiplication and denotes the start of the proportional counting regime. The mechanism by which gas multiplication occurs is called a Townsend Avalanche or a Townsend Discharge. Townsend discharges occur as a function of electron mean free path and anode electric field strength. If the electron mean free path, meaning the distance the electron can travel within the tube before striking a gas molecule, is too short, the the electron will not have sufficient time to gain enough kinetic energy for ionizations. Similarly, if the anode voltage is insufficient the resulting electric field will be unable to accelerate the electrons to the required velocities for ionizing the detecting gas. For Townsend discharges to occur the electrons must have a long enough path along which to travel, and a large enough accelerating field to gain energy before striking a gas molecule. It is for these reasons that the operating region of a GM tube is determined by the combination of detecting gas pressure and applied anode voltage. Like with an ionization chamber, proportional counters produce current signals with magnitudes that are directly proportional to the initial number of ion pairs. Where a proportional counter differs from an ionization chamber is in their output signals; since each ionization in a proportional counter produces an avalanche, the resulting output will be a discrete pulse of charge reaching the anode wire simultaneously. The pulse magnitude is proportional to the number of ion pairs produced, scaled by what is known as the multiplication factor. Proportional counters in IPES experiments have typical gas multiplication factors of 10^2-10^4.

A useful property of proportional counters, that makes them the ideal configuration for IPE experiments, is the fact that the gas multiplication is small enough for the resulting avalanches to remain localized near the initial ionization. This means multiple ionizations can lead to an equal number of simultaneous avalanches, which each produce a discrete output pulse. In the terms of radiation detectors, proportional counters are said to have a zero dead time. In contrast to this, as the anode voltage is further increased the tube passes through a region of limited proportionality, which is still acceptable for use in IPES,

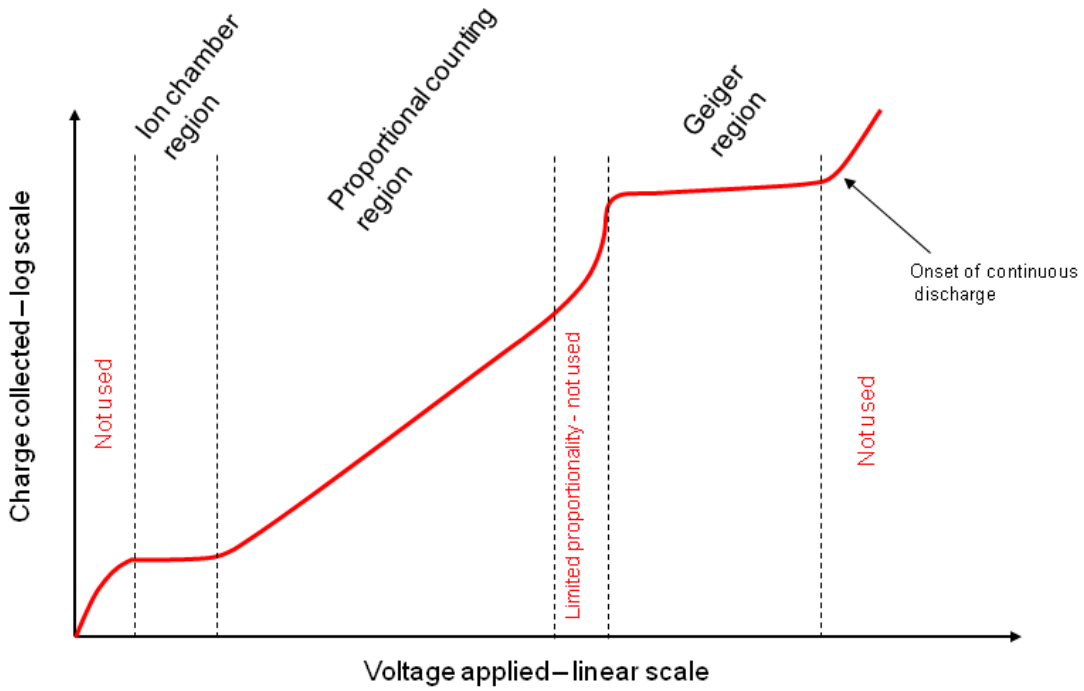


Figure 4.2: Charge collected at the output of a GM detector as a function of applied anode voltage at a constant fill gas pressure. At low anode voltage recombination is suppressed but gas multiplication has yet to begin, the detector is acting in the ion chamber region. As the anode voltage is further increased gas multiplication begins and the detector is working in the proportional region, which is the most common operating mode for IPES. Increasing the anode voltage beyond this puts the detector into geiger mode where gas multiplcation is only limited by the positive space charge buildup from the ionized acetone. Pulse heights are uniform and there is a significant dead time where recombination needs to occur before the tube can be sensitive to photons again. This dead time makes the detector poorly suited poorly suited for IPES applications which has an already very small count rate. Beyond the geiger region dielectric breakdown occurs which is both unusable and potentially damaging to detector electronics. Care should be taken when characterizing a detector to minimize tube breakdown. Taken from [37] under CC Attribution Share-Alike 3.0/Cropped from original.

and enters the final useable region for gas filled detectors: the Geiger region. Unlike in a proportional counter, the avalanches in geiger mode detectors are no longer localized and occur along the majority of the anode wire. Due to this, the only factor capable of stopping the avalanches in this configuration is the build up of positive charge from the ionized detection gas molecules, which in effect supresses the electric field from the

anode wire. Once the multiplication is terminated the tube is completely insensitive to incoming radiation due to a lack of available gas molecules to undergo multiplication. Tubes in Geiger mode therefore have a non-zero dead time where the ion pairs undergo recombination before the system is ready to detect another photon. Further, since the amount of positive charge required to suppress the electric field is a constant for a stable tube, the output pulse heights for a tube in Geiger mode are of roughly equal height and are no longer dependent on the initial amount of ion pairs. Typical gas multiplication factors for geiger tubes are 10^8-10^9, considerably larger than that of proportional counters. A non-zero dead time means that a considerable amount of the incident photons in an IPES experiment will be lost, thus further reducing count rates and increasing the amount of time required to complete a measurement. Thus the ideal configuration for a GM tube in an IPES experiment is the proportional or limited proportional region, with a zero dead time to maximize the detector's efficiency and the resulting count rate.

4.1.2 Achieving UV Energy Sensitivity

As has been mentioned several times previously, GM tubes are used specifically for the technique isochromat IPES, which means they must be engineered in such a way that they are sensitive only to UV photons. Achieving this is done through the creation of a band pass detector, where the width of the band of energies the detector is sensitive to determines its resolution. Recall that we use end-window type detectors, where photons enter through a window of some transparent material, and ionize a detection gas within the tube. We thus have two parameters which can be tuned in order to create a band-pass filter: the ionization energy of the detection gas, and the transmission cutoff of the entrance window. In order for the photons to first make it to the detection gas, the must pass through the entrance window, this implies that the window transmission should set the upper limit of the band-pass, thus the entrance window should act as a low-pass filter. With this in mind, we then need to choose a detection gas with a photoionization yield that is non-zero only for energies near-to and greater than the transmission cutoff of the window, in doing this we use the detection gas as a high-pass filter.

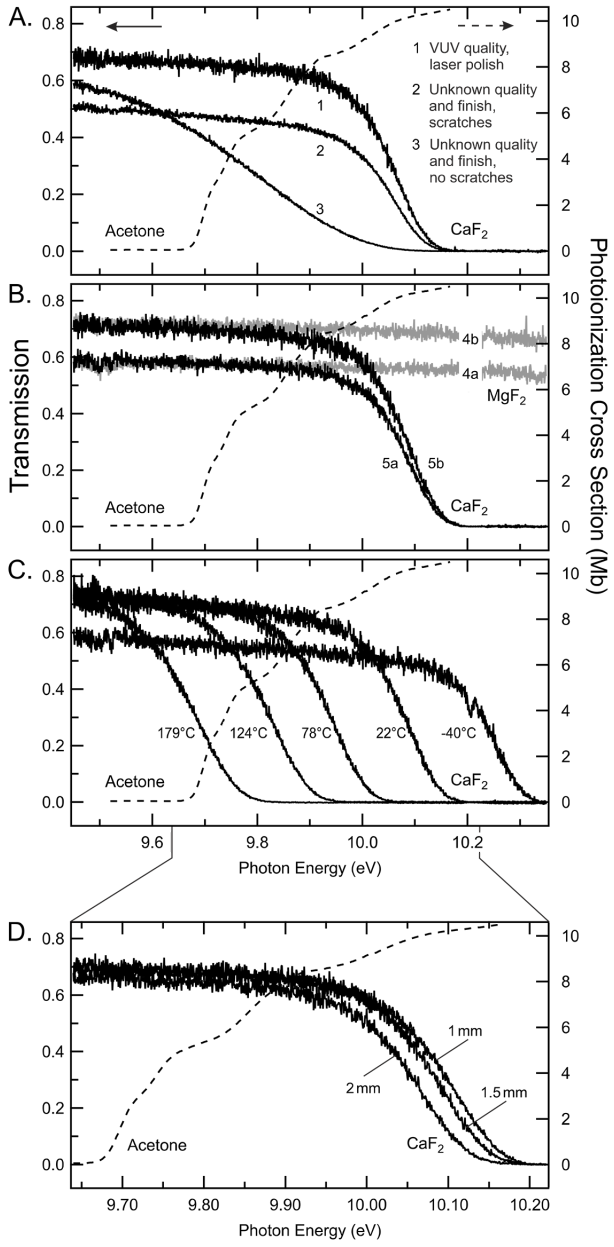


Figure 4.3: Photoionization yield of acetone and optical transmission of CaF_2 as a function of: a) crystal and surface quality b) surface contamination c) temperature d) window thickness. The response function of a gas filled detector with this configuration is created by the high-pass filter from the acetone photoionization and the low-pass of CaF_2 transmission. The width of the response function for the highest quality crystal at room temperature is 325 meV with a detection energy of 9.9 eV. Reprinted from [38], with the permission of AIP Publishing.

Over the history of UV IPES, many combinations of detecting gas and window material so that the resulting band-pass filter is sensitive only to a narrow region of high energy UV photons. The most commonly used detection gases are: I_2, acetone, ethanol, isopropanol, and dimethyl ether. The most common window materials combined with these materials are: MgF_2, CaF_2, SrF_2, and $CaSrF_2$ [38]. For the sake of brevity, this thesis will include only a discussion of CaF_2/acetone, and MgF_2/acetone detectors which are both employed in our lab. The transmission cutoff for CaF_2 is 10.2 eV, and the photoionization threshold for acetone is 9.7 eV, tubes of this configuration are senstive to photons of an energy of 9.8 eV, with a band-pass magnitude of roughly 400 meV. The transmission cutoff for MgF_2 is larger at 11 eV, which yields detectors band-pass magnitudes of roughly 700 meV when paired with acetone as a detection gas [38]. The size of the band-pass is solely responsible for the energy resolution of the detector and thus impacts the spectrometer's ability to resolve the location of unoccupied states. The detector response function, that is the count rate of the detector as a function of photon energy, can be measured using a variable energy VUV source. Response functions for different CaF_2 are shown in Fig. 4.3. One can then extract the width of the response function to estimate the energy resolution of the detector. Sadly we do not have such a source, meaning that a direct measurement of the energy resolution of our detectors is not currently possible. However, the detector energy resolution, combined with the thermal distribution of the electron gun, creates an overall energy resolution of the spectrometer which can be quantified through a variety of experiments. It should be noted that minimizing the band-pass is not always the optimal choice: samples which may be sensitive to prolonged exposure to an electron beam will benefit from reduced measurement times, which can be achieved by large band-pass detectors at the cost of energy resolution. This also applies for reactive samples or unstable samples that even in UHV have a reduced lifetime. This trade-off is why we employ both a CaF_2 detector and an MgF_2 detector, it allows for the choice between high resolution for serious scans, or faster measurement times for preliminary works. The quality of both of these window materials of the utmost importance and we use 157 grade MgF_2 and CaF_2 windows for our detectors. Fig 4.3.a shows the impact of window quality on the resulting transmission and thus response function.

4.1.3 Signal Processing

In this section, I will detail both the general considerations for processing the output signals of proportional counters, and will also describe the specifics of our setup outlining the function and purpose of each component. The first step is converting the current signal to a voltage signal thus allowing it to be fed into a counter card or an ADC later on. The most common choice to accomplish this task are op amp integrators, which are circuits that output a voltage signal that is proportional to the input signal integrated over time. For radiation detection we specifically use what are called charge sensitive preamplifiers

(CSP), meaning that the output a voltage signal which is proportional to the time integral of the input current signal. The charge flowing from a proportional counter is typically very small making the signal highly susceptible to noise, by first amplifying it the signal becomes more robust and can be more easily processed. These CSPs have an associated gain that is typically expressed in units of V/pC, and are engineered to have a stable gain that is unaffected by characteristics of the detectors. CSPs have a very fast rise time, but due to their nature are followed by a relatively very long decay time that is determined by its RC time constant. For example, in our setup employing *Cremat Inc* CR-110s, the stated time constant is 140 μs [39]. As one can imagine this can lead to a potential pileup of signals if one has a detection rate that is greater than once every 140 μs which makes the task of discriminating pulses very difficult. To counteract this we further process the CSP output using what is known as a shaping amplifier.

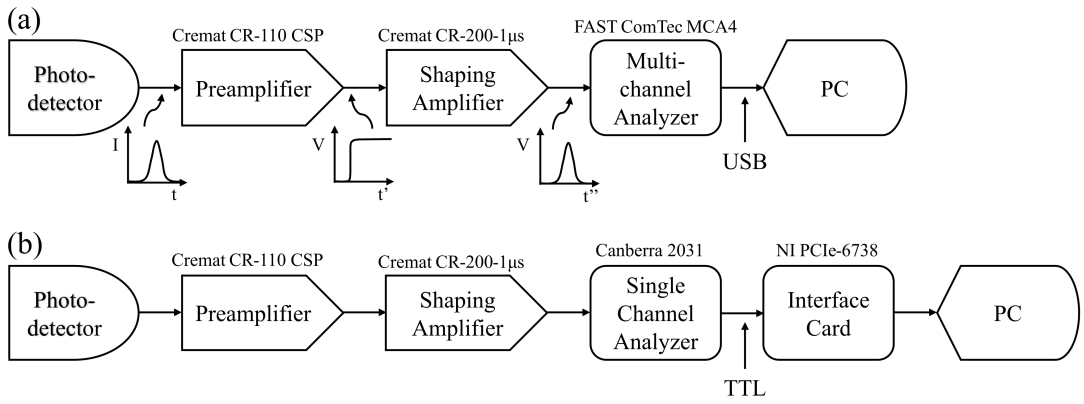


Figure 4.4: a) Block diagram showing our signal processing setup when we are processing signals using a multichannel analyzer. A current pulse from the photodetector is sent through a Cremat CR-110 charge sensitive preamplifier that integrates the input signal. This is fed into a Cremat CR-200 shaping amplifier with a 1 μs shaping time to output a gaussian pulse. The FAST ComTec MCA4 counts the number of these pulses above a minimum threshold height and outputs that to our PC over USB. b) Adapted signal processing block diagram when we are using a Canberra 2031 single channel analyzer in place of our MCA. The SCA outputs a TTL signal when it detects a gaussian pulse within a certain height window, which we feed into an NI PCIe-6738 interface card. Either approach is entirely valid for applications in IPES, however an MCA has an advantage for characterizing detectors by granting access to pulse-height distributions that can be used determine the gas multiplication factor of the detectors.

In our specific use case, shaping amplifiers produce a quick, noise reduced pulse corresponding to the rising edge of the input. In this way shaping amplifiers are able to output essentially discrete pulses corresponding to individual detections, which can then

be fed into discriminators or pulse height analyzers. Shaping amplifiers have an associated constant gain expressed in units of V/V, meaning that the final pulse amplitude is still proportional to the current produced from the initial formation and amplification of ion pairs. These Gaussian pulses have a non-zero width which is typically on the order of a few microseconds [40], much less than the 140 μs from the CSP; thus signal pileup and electrical noise are no longer an issue for counting frequencies less than 1 MHz which is unobtainable in an IPE experiment. Additionally, shaping amplifiers can filter high and low frequency noise such which can originate from sources like the 60 Hz line frequency or mechanical vibrations from vacuum pumps. Therefore shaping amplifiers not only increase out sensitivity to genuine counts but reduce our sensitivity to false counts.

These pulses can then be fed into counting electronics such as pulse height discriminators, multi channel analyzers (MCA), or into a computer for software analysis. For simply performing IPE measurements a pulse height discriminator and an oscilloscope are sufficient. One can determine the pulse height to set the discriminator to using the scope and then count the number of detections in a given amount of time to quantify the IPE intensity. A drawback of using this approach is that it becomes impossible to examine the distribution of pulse heights coming from the detector which is a vital piece of information for characterizing the operating regime of a GM tube. For this reason we choose instead to use an MCA, which is able to discriminate pulses and record their height. As will be seen in the following section, this pulse height data can then be used to determine the operating mode of the detector, as well as the corresponding gas multiplication. Fig. 4.4 shows a block diagram of our signal processing setup, including the names of components and actual oscilloscope traces at varying points in processing.

4.2 Detector Characterization

4.2.1 Operating Mode

The tuning procedure of our detectors is described in a previous work [12], so here I will focus mainly on analyzing the results and will only briefly describe the experimental method applied. Our goal was to tune both detectors to achieve a suitable sensitivity to VUV photons, with minimal so-called dark counts. Dark counts are detections which are not caused by photons, and can be caused by a variety of factors such as corona discharge. A suitable configuration is determined by examining the count rate at varying anode voltages and pressures both in the presence of VUV photons and without. To generate the photons we used a Cu (111) target and a beam energy of 15 eV, we found that while this did not correspond to a specific unoccupied state the associated background count rate provided enough photon intensity for testing.

Due to a malfunction of our MCA, the data presented in this chapter is from our

previous attempts at characterizing our detectors [12]. This is worth mentioning for the fact that the pressure readings were done using a Pirani gauge and were presented as uncorrected N_2 pressures. We have since switched to using capacitance manomters (CM) for acetrone pressure measurements, which are able to measure an aboslute pressure value and require no correction. What was previously reported as a pressure of 3 torr when using a Pirani gauge is actually closer to 5 torr as measured with a CM gauge.

Through multiple iterations a stable configuration for both detectors was found to be 3.7 torr acetone pressure with an anode voltage of 800 V. We then exposed the tubes to VUV photons released from a Cu (111) surface undergoing IPE at an electron energy of 15 eV and recorded the resulting pulses for 100 s. We recorded 134421 total pulses during that time, for an average count rate of 1.34 kHz.

The pulse height distribution of a proportional counter can be modeled using an exponential decay [17] due to the fact that there is significant variance in the gas multiplication of proportional counters, which is directly reflected in the variance of pulse heights of single photon detections like is seen in IPE [38]. We can extract the mean pulse height to determine the average gas multiplication using the known gain of the shaping- and preamplifiers, and the fact that each avalanche begins with a single ion pair [38] according to:

$$\bar{h} = e\bar{M} \times \mathbf{GAIN}_{\text{pre}} \times \mathbf{GAIN}_{\text{shape}} \tag{4.1}$$

To begin, we found that the average pulse height for the CaF_2 was 97.7 mV. Using the manufacturer provided data sheets we determined that the total gain of our electronics was 14 V/pC [39, 40], which can alternatively be expressed as $2.24{\times}10^{-6}$ V/electron. From this we obtain an estimate for the average gas multiplication factor of $\bar{M}_{\text{CaF}_2} = 4.5 \times 10^4$, which is well within the typical range for proportional detectors. We then repeated this for the MgF_2 detector which has a calculated average pulse height of 78.7 mV and yielded an average multiplication factor of $\bar{M}_{\text{MgF}_2} = 4.4 \times 10^4$, once again indicating a detector operating in the proportional region.

To further strengthen this notion we observe near identical gas multiplication factors in both tubes under identical conditions. The effects of tube construction and fill gas are modeled in the Diethorn equation [36]:

$$\ln M = \frac{V}{\ln(b/a)} \frac{\ln 2}{\Delta V} \left(\ln \frac{V}{Pa \ln(b/a)} - \ln K \right), \tag{4.2}$$

where V is the applied anode voltage, a is the anode (wire) radius, b is the cathode (tube's inner) radius, P is the acetone pressure, and K and ΔV are constants determined by the fill gas. Qualitatively from this, we see that for tubes of similar geometry, with similar

fill pressures and anode voltages, the resulting gas multiplication should be comparable. There are slight construction differences between the two detectors, to do with anode wire insulation and stabilization though the relevant parameters for the Diethorn model are identical between the two. This implies that we should observe near identical gas multiplication factors for both detectors. This leads to the conclusion that our estimate for the mean gas multiplication is accurate for both detectors and they are in fact operating as proportional detectors.

As a final note, we observed a significantly lower count rate of just 300 Hz when measuring with the MgF_2 detector compared to the CaF_2 detector which is the exact opposite of what we would expect. The larger band-pass of the MgF_2/acetone system should be allowing in more VUV photons and thus for the same intensity should yield more counts. This is an indication there is an issue with the tube causing a reduced sensitivity. This could be due to a number of factors including: the electric field only being strong enough for gas multiplication along a small portion of the anode wire, window material band gap being smaller than expected, issues with the counting electronics, or inaccurate detector configurations. Due to our previously mentioned MCA malfunctions we have been unable to perform the tests required to determine which of these factors is responsible for the reduced count rates; despite this we have shown that the detector is still capable of producing a sufficient count rate within the proportional region making it suitable for future IPE applications.

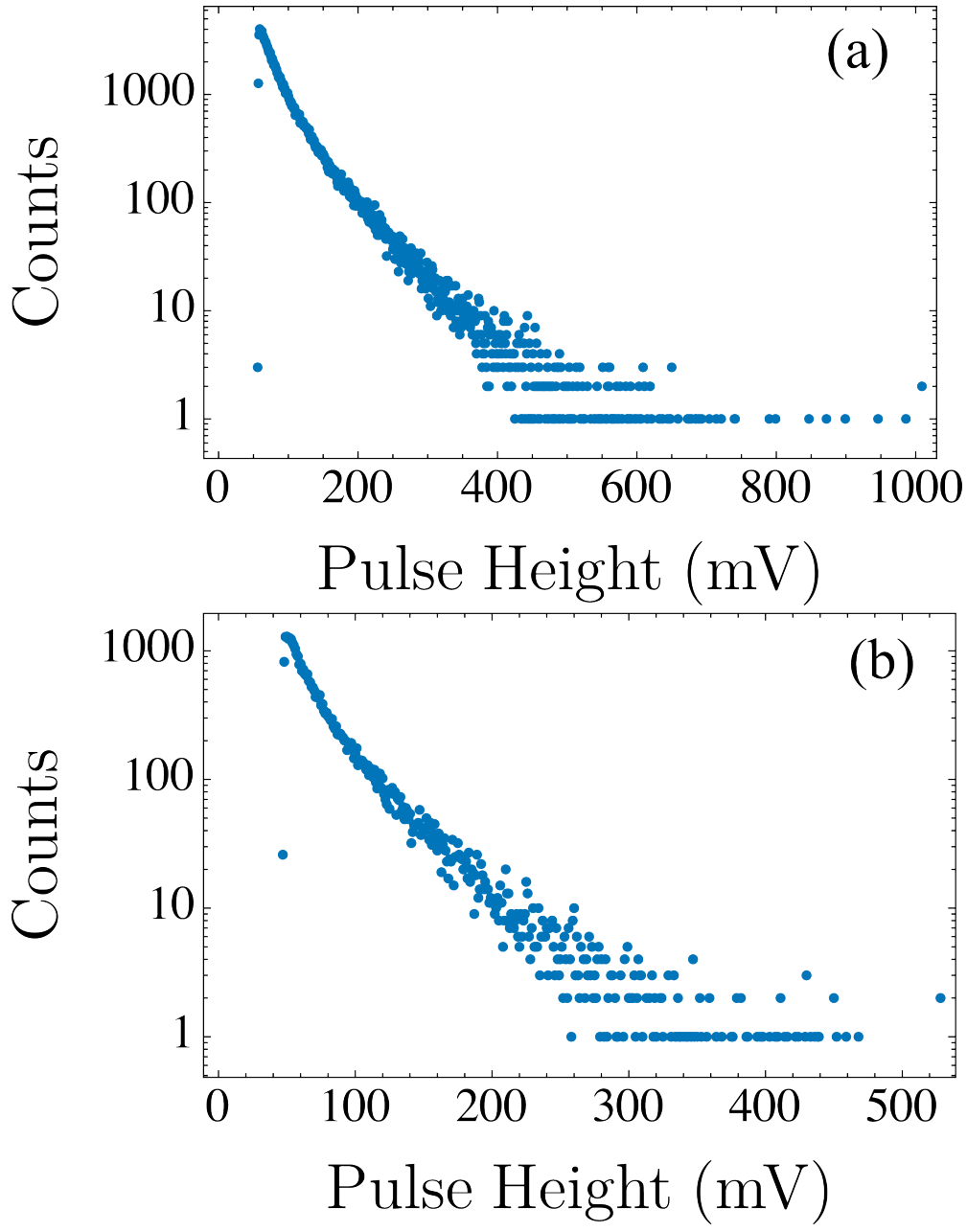


Figure 4.5: Pulse height distributions for a) the CaF_2 and b) MgF_2 detectors. The MCA bins the incoming pulses and records the number of pulses in each bin. For detectors in the proportional region we expect an exponential decay for the pulse heights and by determining the average pulse height we are able to estimate the average gas multiplication factor.

Chapter 5

Spectrometer Energy Resolution

The energy resolution of an IPE spectrometer is one of a few metrics which can be used to quantify its performance. In essence, it describes how well the system is able to determine the energy of an unoccupied electronic feature. There are many factors which affect the energy resolution a spectrometer is able to obtain however only two of them are from the system itself, those being: the thermal and space charge energy broadening of the electron source and the width of the detector response function. There are sample specific factors which also influence resolving ability, such as thermal broadening of the Fermi edge and lifetime broadening of image potential peaks which will both be discussed later in this chapter. It is almost always a valid assumption however that the broadening associated with the spectrometer itself is at least one if not two orders of magnitude larger than these contributions.

There are a multitude of ways in which an experimenter could determine the energy resolution of their system. The best approach is to directly measure both the energy distribution of the electron beam using a device like a retarding field analyzer [41], and the detector response function by examining count rate as a function of photon energy using a variable VUV photon source normalized to the photon intensity [41, 42]. The total energy resolution can then be estimated using a quadrature addition of these two values [43]. The issue with this approach is that it requires a large amount of extraneous equipment which will most likely be used only once. A second, much simpler approach, is to simply directly measure how broad a known feature is compared to its width if one had used a spectrometer with a perfect energy resolution. This approach is a compromise since it allows one to directly estimate their spectrometer resolution using their already established setup, at the cost of no longer being able to discuss the performance of individual components. Due to its simplicity the second approach is more commonly used and thus there are a variety of accepted samples and their corresponding features which the community uses for characterization. It should be noted that this discussion is relevant only to our CaF_2 detector,

our MgF_2 detector was experiencing instabilities which meant we could not perform these same experiments with it. If we were able to measure with the MgF_2 detector, one would expect to obtain a larger energy resolution and greater IPE intensity due to the increased width of the detector's response function.

5.1 Fermi Edge of Metals

The first feature commonly used to estimate enery resolution is the Fermi edge of metals [41, 44, 14, 17]. This is done because at finite temperatures there is a non-zero density of states (DoS) at the Fermi level, making it accessible to IPES [14]. If one were to measure the Fermi edge with a spectrometer of perfect resolution, the photon intensity as a function of electron energy, $I(E)$, would be given by:

$$I(E) = [1 - n_{\mathrm{FD}}(E, T)]\,(a + bE) \tag{5.1}$$

Where $1 - n_{\mathrm{FD}}(E, T)$ is the empty state Fermi function at energy E and temperature T, and $a + bE$ is a linear background which reflects the typically linear DoS of metals near the Fermi energy, combined with the constant dark counts from the detector. To account for the non-zero energy resolution of the detector this intensity function is then convolved with what is known as the spectrometer resolution function, $G(E)$, which is typically approximated as a Gaussian function with width determined by the experimental energy resolution. This gives an expected signal function, $H(E)$, that can be expressed as:

$$H(E) = ([1 - n_{\mathrm{FD}}(E, T)]\,(a + bE)) * G(E) \tag{5.2}$$

The issue is that the function $H(E)$ has no closed form meaning that it is very difficult to fit it to experimentally observed data. To account for this we choose to modify the expected intensity function to the form:

$$I'(E) = [1 - n_{\mathrm{FD}}(E, 0)]\,(a + bE) \tag{5.3}$$

Which is simply using the zero temperature Fermi function instead of the finite temperature version. The advantage of this is that we now have a closed form expression for the expected signal function:

$$H(E) = \left[1 - \mathrm{erf}\left(\frac{E_f - E}{\sqrt{2}\sigma}\right)\right](a + bE) \tag{5.4}$$

The drawback of this approach is that we have removed the contribution of thermal broadening and have absorbed it into the width of our resolution function, σ. To compensate for this we assume that the thermal broadening adds in quadrature and simply subtract off the roughly 25 meV contribution at 20°C. Note that since these uncertainties add in quadrature the effect of the thermal broadening on the energy resolution should be small.

The first sample we used for this method was a polycrystalline gold foil which we first treated with ultrasonication in a solution of oxide remover. We then mounted it on a copper sample plug with a background of Aerodag® G, secured by means of conductive silver paint. This is the same sample depicted in Fig. 3.8.a. The sample was then transferred to our UHV preparation chamber so that its surface could be further cleaned using Ar^+ ion bombardment. We used a base Ar pressure of 5×10^{-6} torr at a beam energy of 1 kV. The sample was etched for a total of 30 minutes, however due to technical issues could not be annealed. We attempted to perform LEED to determine suface quality but no polycrystalline diffraction pattern could be obtained. This most likely indicates extensive surface roughness due to the aforementioned lack of annealing.

The sample was then transferred to our main IPE chamber, where five spectra were taken sequentially. Each point is the result of a 10 second integration time over an energy range of 4 eV using a step size of 0.05 eV. The spectra were then averaged to produce the results seen in Fig. 5.1.

From fitting to equation 5.4 we extracted an energy resolution of 410 meV. By subtracting of the contribution of thermal broadening we arrived at a final estimate for our experimental energy resolution of 400(60) meV. From this fitting procedure we were also able to determine the location of the Fermi energy for our system of 6.9 eV which can be used for subsequent measurements.

We then repeated this procedure for a 10 mm $\times$ 10 mm sample of single crystal Cu (111) The sample was large enough that we did not need a graphite background and we were able to anneal the sample at a temperature of roughly 500 °C for several hours. This time a very sharp and well defined LEED pattern was observed which indicates a smooth and well ordered surface. We performed IPE measurements at normal incidence which was done to prevent the image potential state from influencing the shape of the Fermi edge. At $k_{||} = 0$ Å^{-1} ($\theta = 0°$) the image potential state disperses below E_f and thus is inaccessable to IPES [45]. Despite this there is still an observed peak at 0.2 eV above E_f which is attributed to the Shockley surface state which is detectable at normal incidence [43].

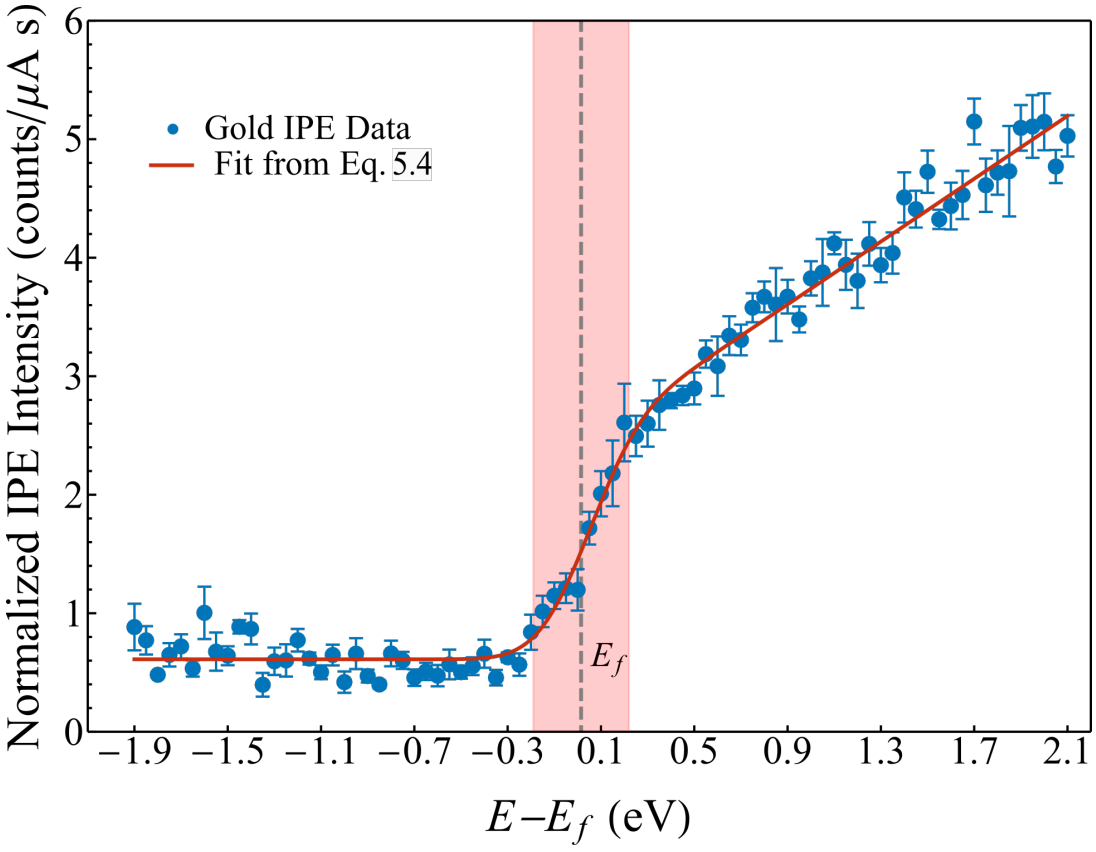


Figure 5.1: IPE measurement on Gold foil near the Fermi edge and fit to eq. 5.4. Error bars are mean-squared error (MSE) from averaging the results of 5 IPE spectra with integration times of 10s per point. Normalization of data was performed using the results found in Fig. 3.4.

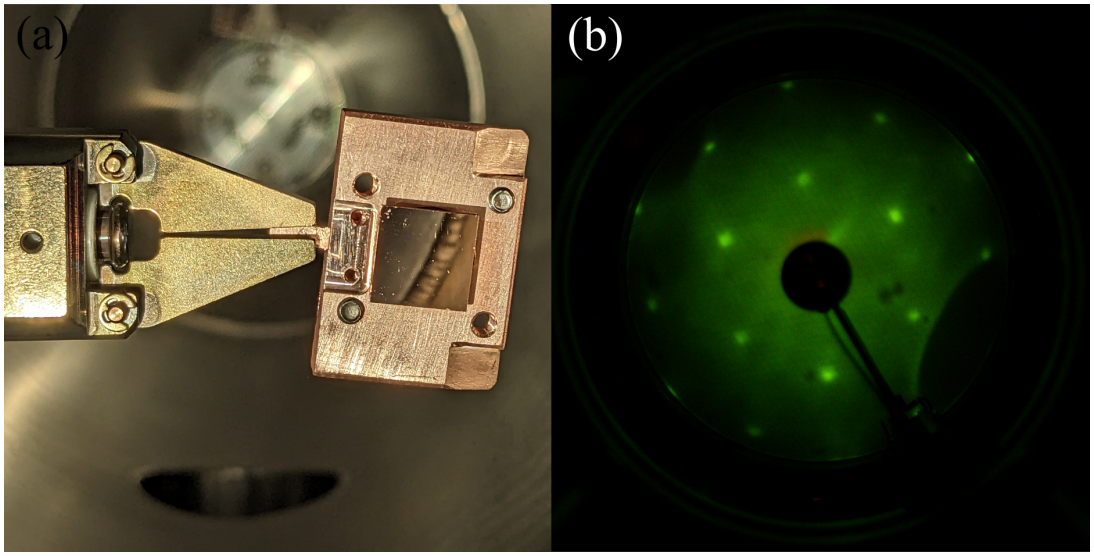


Figure 5.2: a) Freshly prepared Cu (111) sample in our preparation chamber. b) Obtained LEED spectrum showing the 6-fold symmetry of the FCC (111) surface Brillouin zone. This, combined with the sharp peaks, indicated that the sample's surface is sufficiently clean and ordered for IPES.

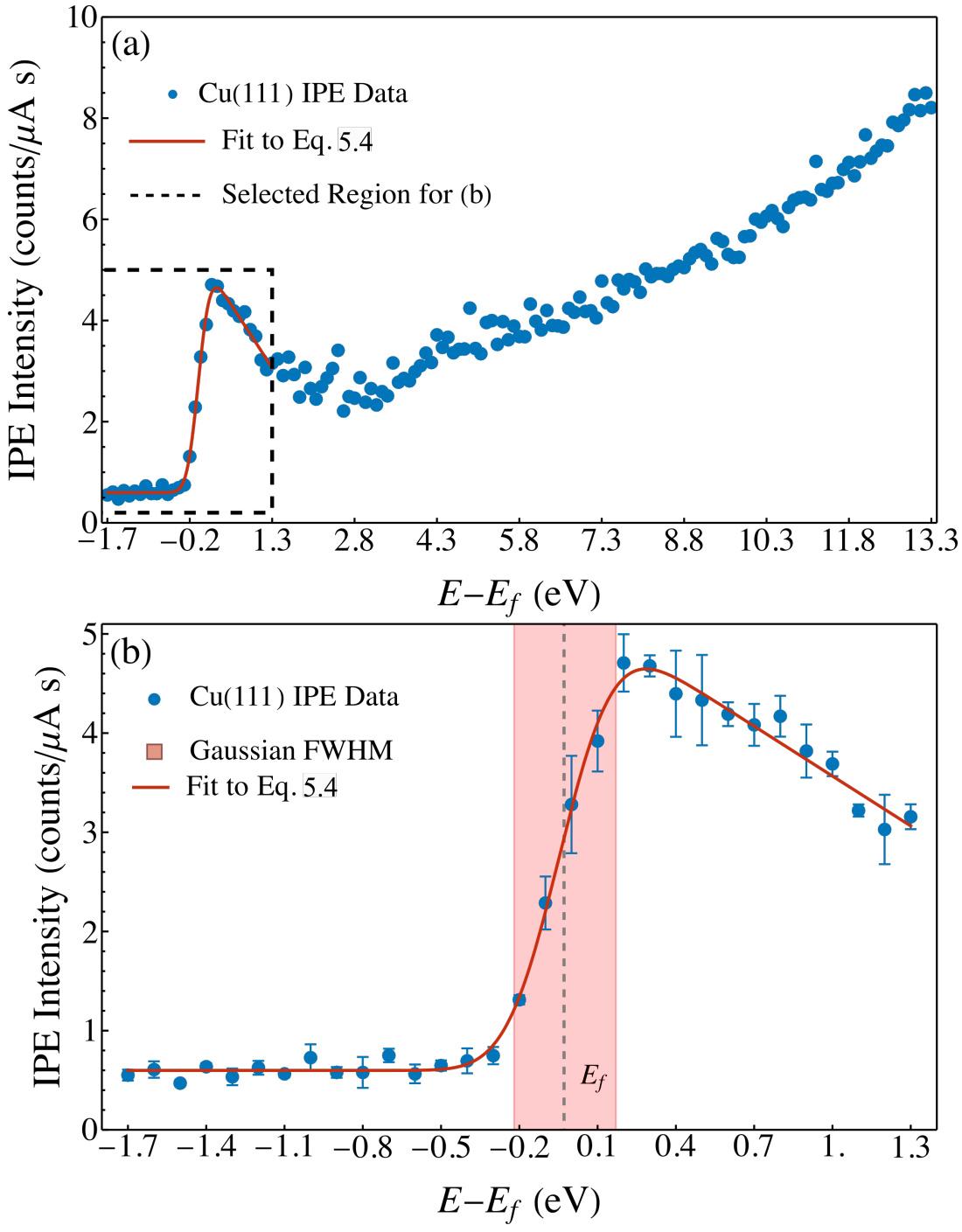


Figure 5.3: Full IPE spectrum of Cu(111), boxed area is region around E_f which is used for fitting to eq. 5.4, red curve is the resulting fit. b) Zoomed in view of boxed region. Error bars are MSE from averaging 10 scans each using a 10s counting time. Red line is the fit to eq. 5.4, and the red shaded area is a visualization of the resolution function's Gaussian FWHM centred on E_f.

Performing the same fitting procedure to the data contained in Fig. 5.3.b we were able to extract an estimate for our experimental energy resolution of 388(25) meV. If we combine the results of both estimates we find that a lower bound on our energy resolution is 360 meV and an upper bound of 460 meV, to see how this compares we can compute an estimate for the energy resolution for our system. First we use the band-pass width of 320 meV from [38], then a rough estimate for the electron thermal energy broadening of 260 meV [46] from a hot cathode at a temperature of 1200 K. Doing this we obtain a value of 412 meV which implies that our spectrometer is performing exactly as anticipated for our given setup.

5.2 Image Potential States

Another commonly used unoccupied feature for determining energy resolution is the image potential (IP) state. These are used because their inherent lifetime broadening is typically two orders of magnitude smaller than the energy resolution of the spectrometer, meaning that any observed broadening of these features can be entirely attributed to the spectrometer itself [41]. For example, the $n = 1$ IP state for Cu(111) has a lifetime broadening of just 18 meV [47] which is negligible in comparison to our 400 meV energy resolution estimate. To estimate energy resolution from an IP state, a Gaussian function on a polynomial (typically quadratic) background is fitted and the FWHM of the peak is taken to be ΔE_{exp} [41, 44, 48].

Image potential states are formed by electrons impinged on a surface becoming bound in the potential well formed by their own image charge. They exist for a wide variety of samples meaning that they are very accessible for the purpose of characterizing IPE spectrometers. Ideally we would examine the image potential state of our Cu(111) sample, however we have been unable to successfully resolve it despite numerous attempts. We believe this was most likely a case of bad timing, where our surface was pristine while the detectors were performing poorly and in the time it took for us to optimize them the surface quality had degraded. Image potential states are surface states making them even more sensitive to surface quality than, say, the Fermi edge which as we saw with the polycrystalline gold sample can be resolved even on rough surfaces. This is mentioned to introduce what we have found to be the best sample to characterize an inverse photoemission spectrometer: highly oriented pyrolytic graphite (HOPG). HOPG will be discussed extensively in the next chapter, so for now will only explain what makes it suitable for characterizing our energy resolution.

HOPG exhibits a sharp IP state much like the typically used metallic samples. Unlike metal samples HOPG is a layered material meaning that it can be mechanically cleaved under UHV, which exposes a pristine surface that is ideal for IP state measurements. To prepare the sample we mounted it with conductive silver paint on our usual copper sample

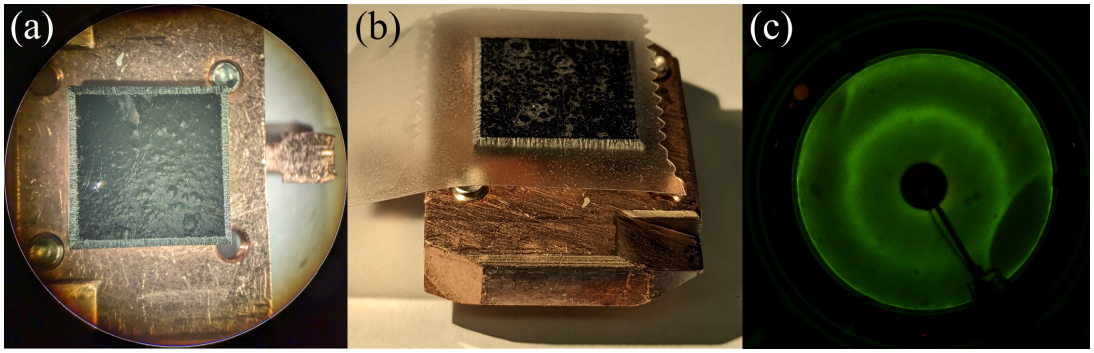


Figure 5.4: a) HOPG sample after a tape cleave performed in atmosphere b) HOPG sample with UHV safe tape applied so it can be cleaved in vacuum c) Resulting LEED pattern showing the characteristic rings expected from a polycrystalline sample.

plug. Once the paint had dried a preliminary tape cleave was performed in atmosphere to remove the orginal surface layer. To this freshly expose surface a second piece of tape was attached and the sample was loaded into the vacuum system. The tape was removed from the surface by means of our sample translation arm. We then performed LEED and obtained a polycrystalline diffraction pattern which was used to align the sample. Fig. 5.4 outlines this process, the annular rings are the hallmark of polycrystalline diffraction.

We then rotated the sample to normal incidence using the correction value determined by LEED and performed IPES over an energy range of 3 eV using an increment of 0.05 eV. Eight spectra were taken and averaged with each point using an integration time of ten seconds.

The data in Fig. 5.5 shows the $n = 1$ image potential peak which we determined to be located at an energy of 3.65 eV above E_f. This is in strong agreement with previous experimental and theoretical work done on HOPG [49, 50], and is a strong indicator that our spectrometer is working as intended. A Gaussian fit to this feature revealed an energy resolution of 379(19) meV. Combining these three estimates gives us our final estimate for our energy resolution of 415(55) meV.

This final estimate contains a contribution from the gold Fermi edge which is both outdated and from a poor quality surface. As an initial quantification of our system's capabilities it demonstrates that we are capable of resolving a variety of unoccupied states, but future refinements of these experiments should be done in order to truly reflect the performance of our spectrometer. This should include a measurement of the image potential and Fermi edge states on both of our newly acquired Cu(111) and Cu(100) samples, and reprocessing the gold foil to produce a better quality surface.

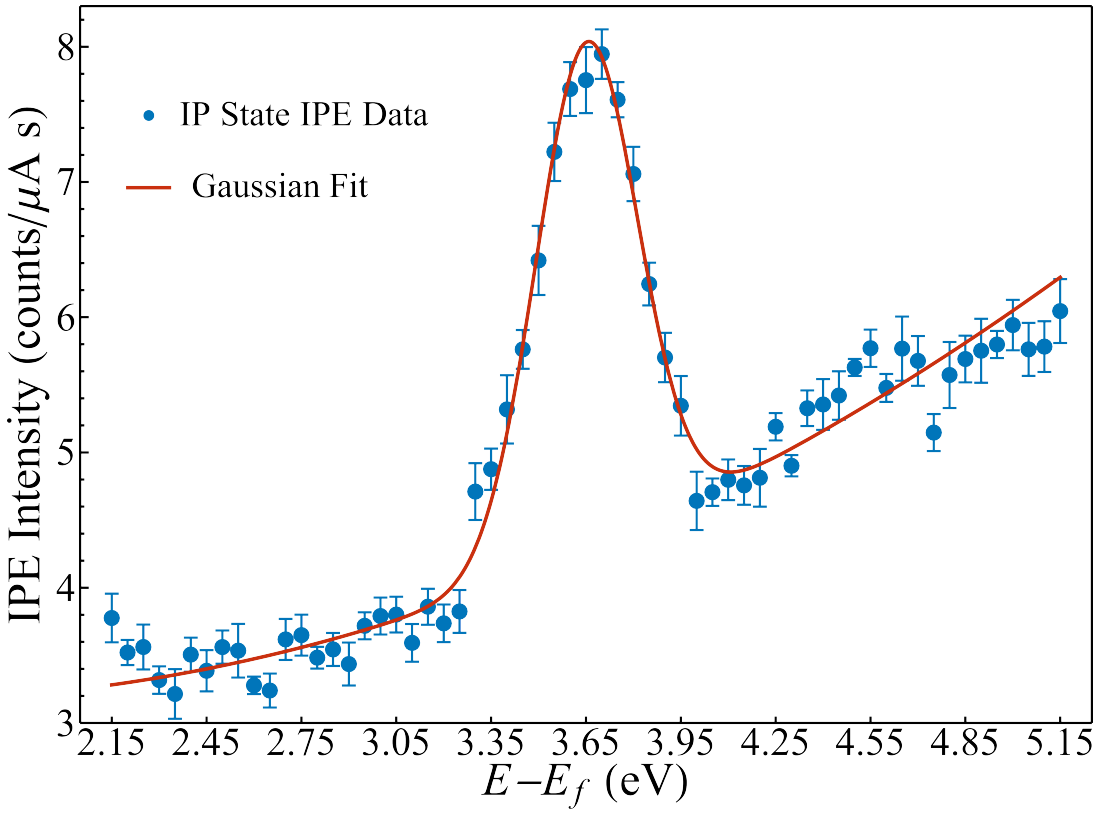


Figure 5.5: Normal incidence measurements of image potential state of HOPG, error bars are MSE from averaging 10 scans each with a 10s couting time. Red curve is the result of least squares fitting to the data using a Gaussian function on a quadratic background. Normalization of the data was done using the total current data show in Fig. 3.4. Note the small hump in the data at 4.55 eV, which can most likely be attributed to higher order members of the IP Rydberg series which our spectrometer does not have the capability of resolving.

Chapter 6

Inverse Photoemssion Study of Highly Oriented Pyrolytic Graphite

HOPG is an amorphous form of graphite with a small mosaic angle between its crystallites. Despite a small mosaic angle each crystallite has a random rotation about an axis perpendicular to the basal plane. As was mentioned previously we have found HOPG to be one of the best test samples for inverse photoemission spectroscopy. First, HOPG cleaves very easily along this plane and can be exfoliated in vacuum just using UHV compatible tape. Once cleaved it is extremely inert in UHV and we have had samples last for over a month which still yielded clear spectra that included a resolved image potential state. Additionally the unoccupied electronic structure of HOPG is very complicated with several highly dispersive features that extend over large portions of the Brillouin zone [51]. Due to the rotational disorder in the basal plane of HOPG we are unable to quantify k_x and k_y meaning that we are probing all states with parallel momentum $k_{||}$ simultaneously.

To perform a full band mapping we first re-cleaved the sample shown in Fig. 5.4 and aligned to its principle axis using LEED. We measured over an angle range of 75° in increments of 5°, and an energy range of 6 eV to 23 eV in steps of 0.1 eV. We repeated this measurement a total of 6 times using an integration time of 10 seconds per point for a total integration time of one minute per point. Fig. 6.1 shows the results of these scans with the data being normalized using the total current interpolation function obtained in Chapter 3.

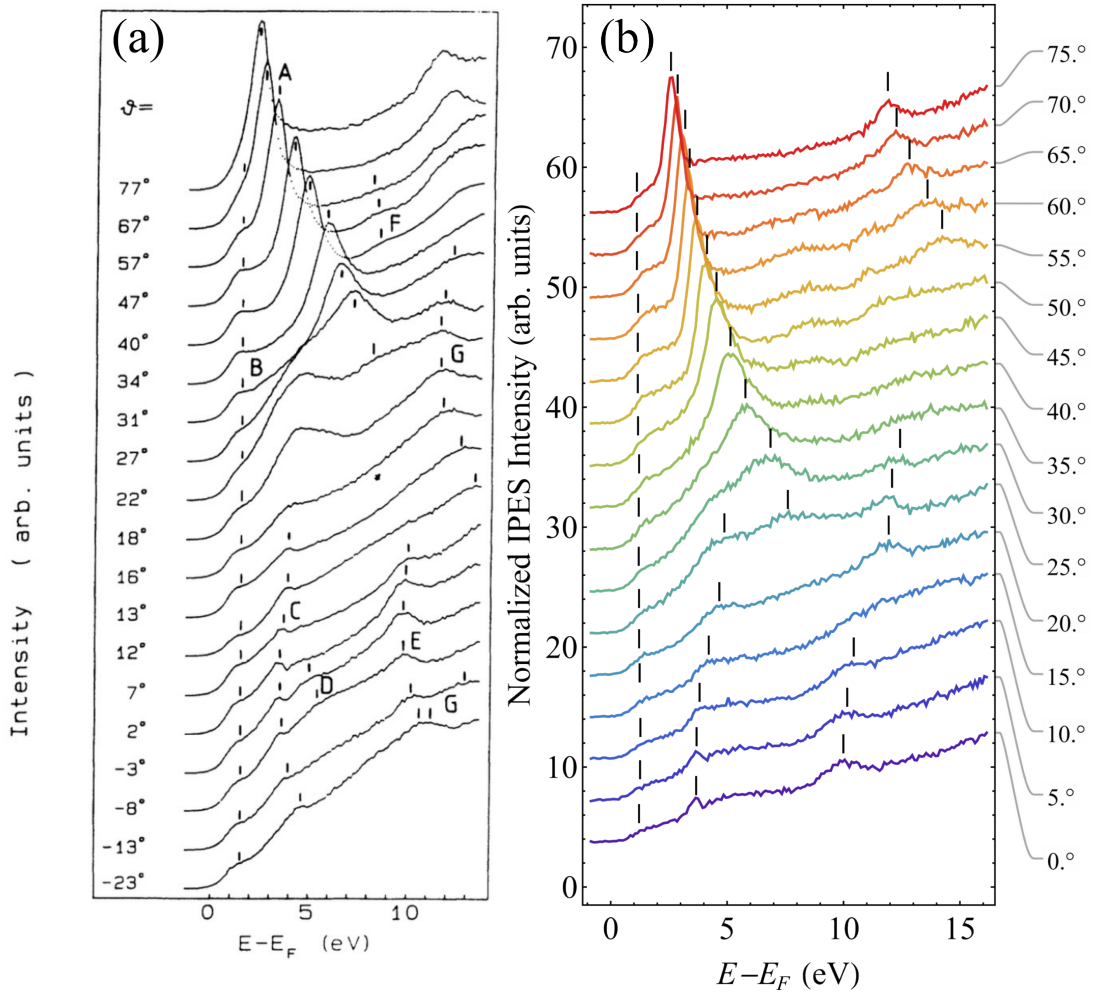


Figure 6.1: (a) Angle resolved IPE spectrum of HOPG obtained from Ref. [50]. (b) ARIPES spectrum of HOPG using our spectrometer, photon intensity data has been normalized using total beam current delivered to sample. Features in both are highlighted with black lines which serve as a guide to the eye. We see strong agreement between the two datasets in terms of feature shape, appearance energy and angle, and dispersive properties. Reprinted with permission from [50] Copyright 2024, American Physical Society

We observe several dispersive features in the ARIPES spectrum with the most apparent being the emission that appears at 75° at an energy of 3.2 eV and disperses upwards with decreasing angle. Ref [50] goes into great detail on the origins of each of these features but explaining the unoccupied electronic structure of graphite is beyond the scope of this thesis. An exception to this is the feature which appears at normal incidence at an energy of 3.85 eV and disperses until an angle of 25° which we will argue is an image potential state. A non-dispersive shoulder is observed at roughly 1.6 eV that persists over the entire angle range. Three other higher energy dispersive peaks are also observed though the do not persist over a very large angle range compared to the other features observed.

Image potential states, as mentioned previously, disperse parabolically (relative to the vacuum level) as a function of $k_{||}$ according to:

$$E_n(k) = \frac{0.85 \text{ eV}}{(n+a)^2} + \frac{\hbar^2 k_{||}^2}{2m^*} \tag{6.1}$$

The quantum defect $a \in [0, 0.5]$ and effective mass m^* reflect the interaction of the image potential state with the rest of the sample [52]. In order to determine if the selected emission is an image potential state we can extract its peak positions and corresponding parallel momenta and perform a fitting to the above dispersion. The results of this fitting are shown in Fig. 6.2 below. It should be noted that this is taken from a dataset which was meant to show the full band dispersion of HOPG and thus the amount of data points which constitute the image potential peak is considerably smaller than in the dataset used for Fig. 5.5. Because of this there is significant room for error in determining the peak positions, additionally we only have a few selected angles over which to perform the fitting. For this reason these results should be taken as preliminary and we will need to perform dedicated measurements with a smaller angle step, reduced energy step size, and over a smaller energy range. Preliminary in this case meaning that it is sufficient to demonstrate that the observed feature is an image potential state, but any claims about the effective mass and quantum defect should be taken with large error bars.

We extracted a $k_{||} = 0$ Å^{-1} band minimum of 3.88(4) eV relative to E_f. In order to determine this state's index in the IP series and corresponding quantum defect we need to determine the binding energy relative to the vacuum level. Since we reference all energy values to the Fermi energy the vacuum level is equivalent to the sample's work function. Ref. [50] outlines an experimental method which can be performed using an IPE spectrometer in order to determine the work function of a sample under test. This is done by applying a slight negative bias to the sample and then measuring the current transmitted through the sample as the electron energy is increased. The onset of transmitted current is then taken to be the sample's vacuum level. At the time of writing we have not performed this measurement so for this analysis we will use the value of $\phi_s = 4.7$ eV obtained by Ref. [50] since we would perform an identical experiment under similar conditions. We

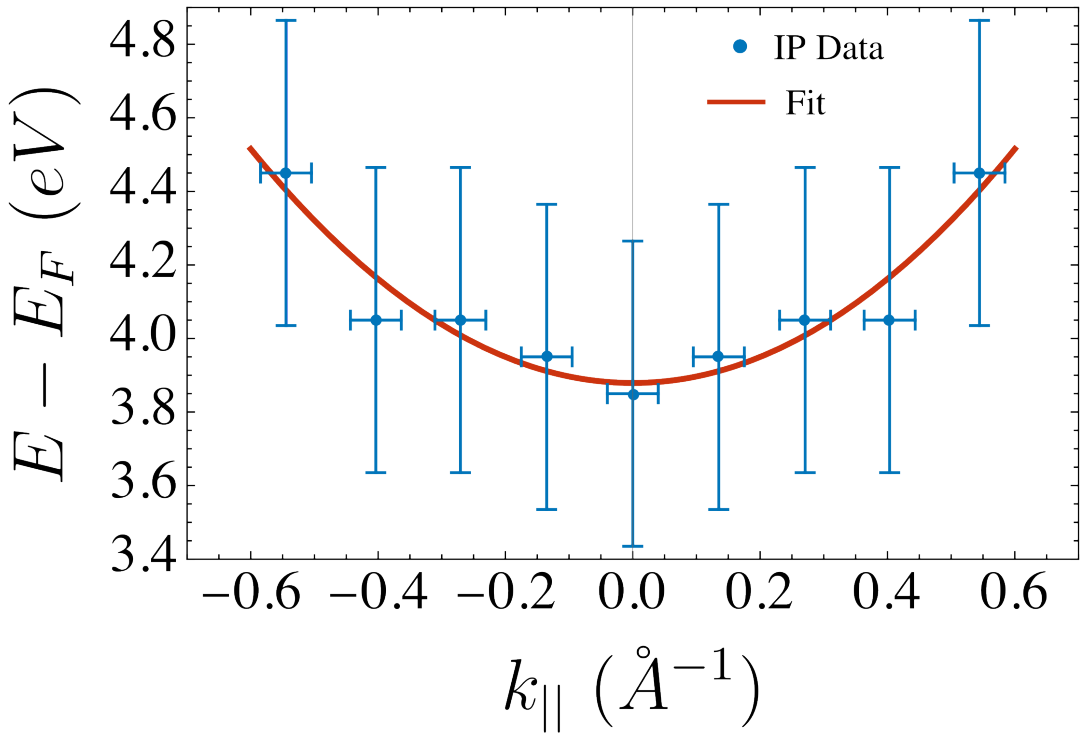


Figure 6.2: Peak positions of the image potential state and the corresponding parallel momentum. Error bars were determined by assuming a beam divergence of 1.5°. A fit using eq. 6.1 was performed in order to determine the band minimum and electron effective mass. Error bars in $k_{||}$ were computed assuming a beam divergence of 1.5° and error bars in E_f are the calculated 415 meV energy resolution of our spectrometer.

thus determine that the binding energy of this state relative to the vacuum energy is 0.8(4) eV. From this we conclude that this state best corresponds to the $n = 1$ image potential state with a quantum defect of 0.018(24) and an effective mass (extracted from fitting) of $2.16(28)m_e$. The effective mass is considerably larger than the one extracted from Ref. [50] at $1.3m_e$. Due to the aforementioned factors we simply do not have enough data to make any conclusions beyond the fact that what we're observing is in fact an image potential state.

In order to determine the parallel momentum values shown in Fig. 6.2 and 6.4 we first needed to measure the contact potential of our HOPG sample. This was done by following the procedure outlined in Chapter 2, using a constant beam energy of 10 eV. The sample bias was then varied in steps of 0.1 V while measuring the resulting transmission current.

The onset of current transmission was found to be at a sample bias of 8.350(5) V,

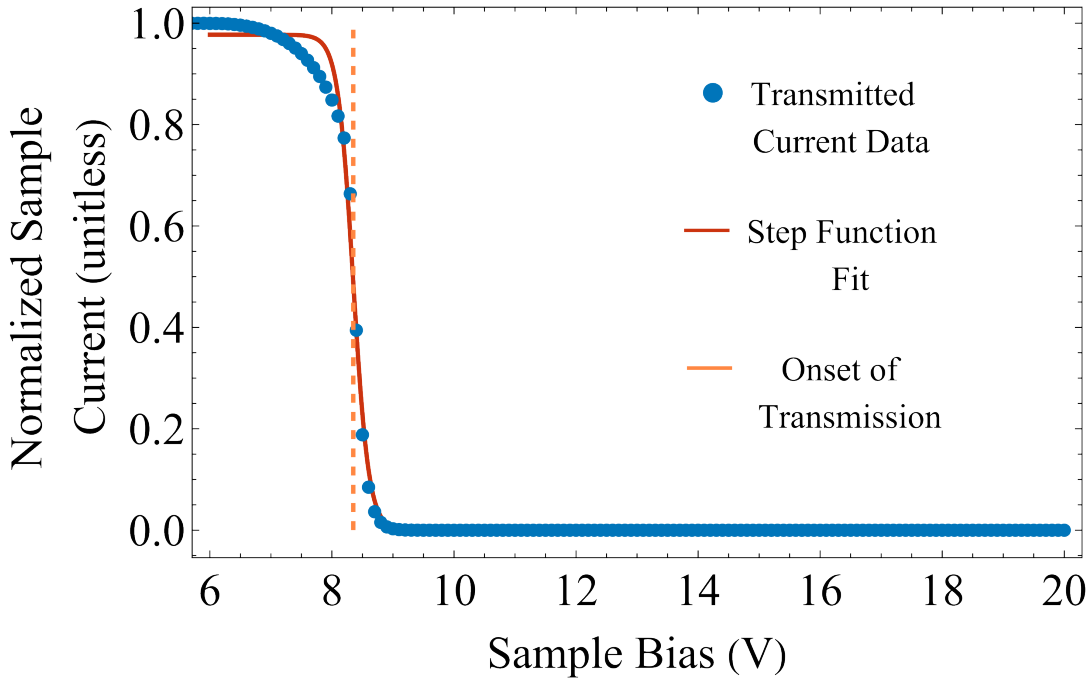


Figure 6.3: Measurement of contact potential for HOPG. The beam energy was held at a fixed 10 eV and transmitted current was measured as a function of sample bias voltage. The fitted function was used to determine the location of the half-maximum value, which is then taken to be the onset of transmission. In the future these measurements will be performed using a smaller voltage step size so that the half-maximum location can be determined directly.

from which we determine that the contact potential for our HOPG sample is 1.650(5) eV which allows us to determine the kinetic energy and thus parallel momentum. Finally, we present an unoccupied band mapping of HOPG to demonstrate that our spectrometer is fully capable of novel IPE measurements.

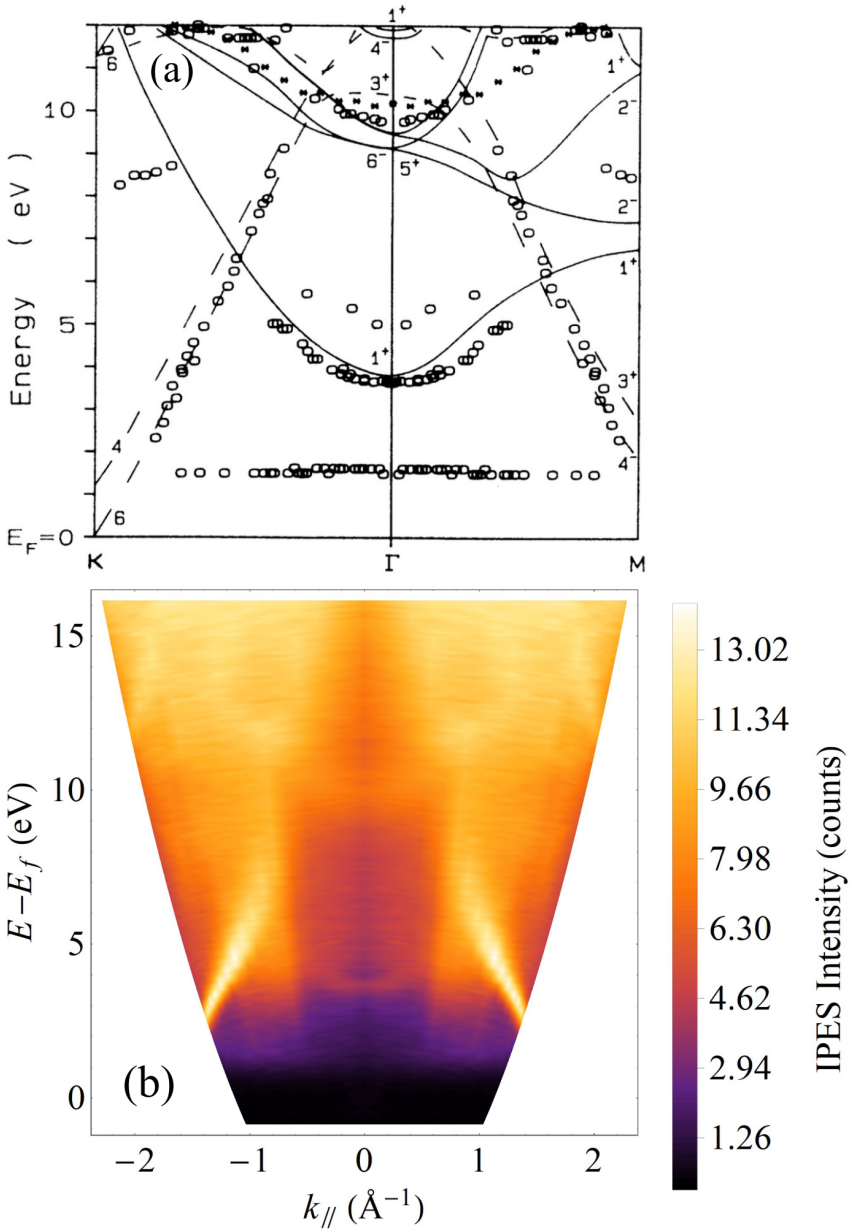


Figure 6.4: (a) Experimental band dispersion for HOPG from Ref [50], using data shown in Fig. 6.1. Overlaid is a computed band structure from Ref. [51]. (b) E-k map for HOPG created by computing the parallel momentum for the data in Fig. 6.1. Note that the map in (b) was produced by symmetrizing the data in Fig. 6.1 about $k_{||} = 0$ Å^{-1}. Reprinted with permission from [50] Copyright 2024, American Physical

Chapter 7

Conclusion

The goal of this project was to characterize the performance of all the relevant components of our inverse photoemission spectrometer. Starting with our electron source we were able to perform Weiner deconvolution of our current intensity data measured with a Faraday cup. By deconvolving the influence of the Faraday cup we were able to extract the total current delivered by the beam as a function of electron kinetic energy. This allowed us to normalize our photon intensity data by the total current delivered to the sample, a vital step in analyzing IPES data.

Using the distribution of pulses produced by our photon detectors we were able to determine that both our CaF_2 and MgF_2 detectors are operating in the proportional region with an average gas multiplication factor of roughly 4.5×10^4.

We were able to determine the energy resolution of our spectrometer by performing IPE measurements at the Fermi edge of both Cu (111) and polycrystalline gold, which yielded results of 388(25) meV and 400(60) meV respectively. Further measurements on the image potential state of HOPG produced an energy resolution of 379(19) meV. This is exactly in line with what we would expect based on our choice of photodetectors.

Finally we were able to produce a full band mapping of the unoccupied electronic states in HOPG. We were able to observe several dispersive features and could perform a fitting to the $n = 1$ image potential state to estimate is binding energy and effective mass. We can safely conclude that we met our goal of characterizing our spectrometer and are now able to perform novel measurements to extract the unoccupied electronic structure of materials.

7.1 Future Work

Our immediate next steps will be finishing some final system preparations and fixing last minute issues. Once this is finished we will immediately start measurements on the topo-

logical insulator Bi_2Te_3 which to our knowledge has not had its unoccupied structure mapped experimentally. We then plan to move to the subject of what will hopefully be my PhD work: the doping dependence of the unoccupied electronic structure of cuprate superconductors.

IPES being so niche makes it incredibly easy to find experiments which have never been performed, so we anticipate having no shortage of measurement opportunities.

References

[1] A. Damascelli, "Probing the electronic structure of complex systems by arpes," *Physica Scripta*, vol. 2004, no. T109, p. 61, 2004.

[2] S. Hüfner, *Photoelectron spectroscopy: principles and applications*. Springer Science & Business Media, 2013.

[3] P. Johnson and S. Hulbert, "Inverse photoemission," *Review of Scientific Instruments*, vol. 61, no. 9, pp. 2277–2288, 1990.

[4] S. G. Davison and M. Steślicka, *Basic theory of surface states*, vol. 46. Oxford University Press, 1996.

[5] A. Tamai, W. Meevasana, P. King, C. Nicholson, A. De La Torre, E. Rozbicki, and F. Baumberger, "Spin-orbit splitting of the shockley surface state on cu (111)," *Physical Review B—Condensed Matter and Materials Physics*, vol. 87, no. 7, p. 075113, 2013.

[6] D. I. Khomskii, *Basic aspects of the quantum theory of solids: order and elementary excitations*. Cambridge university press, 2010.

[7] A. Damascelli, Z. Hussain, and Z.-X. Shen, "Angle-resolved photoemission studies of the cuprate superconductors," *Reviews of modern physics*, vol. 75, no. 2, p. 473, 2003.

[8] N. Armitage, F. Ronning, D. Lu, C. Kim, A. Damascelli, K. Shen, D. Feng, H. Eisaki, Z.-X. Shen, P. Mang, *et al.*, "Doping dependence of an n-type cuprate superconductor investigated by angle-resolved photoemission spectroscopy," *Physical Review Letters*, vol. 88, no. 25, p. 257001, 2002.

[9] S.-L. Yang, J. Sobota, Y. He, Y. Wang, D. Leuenberger, H. Soifer, M. Hashimoto, D. Lu, H. Eisaki, B. Moritz, *et al.*, "Revealing the coulomb interaction strength in a cuprate superconductor," *Physical Review B*, vol. 96, no. 24, p. 245112, 2017.

[10] C. Hu, J. Zhao, Q. Gao, H. Yan, H. Rong, J. Huang, J. Liu, Y. Cai, C. Li, H. Chen, *et al.*, "Momentum-resolved visualization of electronic evolution in doping a mott insulator," *Nature Communications*, vol. 12, no. 1, p. 1356, 2021.

[11] C. McMahon, "Design of an Inverse Photoemission Spectrometer for the Study of Strongly Correlated Materials," Master's thesis, Jan. 2013. Publisher: University of Waterloo.

[12] Y. Qi, "Characterization of Detector and Electron Source for Inverse Photoemission Spectrometer," Master's thesis, Feb. 2023. Publisher: University of Waterloo.

[13] J. Pendry, "Theory of inverse photoemission," *Journal of Physics C: Solid State Physics*, vol. 14, no. 9, p. 1381, 1981.

[14] V. Dose, "Ultraviolet bremsstrahlung spectroscopy," *Progress in surface science*, vol. 13, no. 3, pp. 225–283, 1983.

[15] N. V. Smith, "Inverse photoemission," *Reports on Progress in Physics*, vol. 51, no. 9, p. 1227, 1988.

[16] V. Dose, "Momentum-resolved inverse photoemission," *Surface Science Reports*, vol. 5, no. 8, pp. 337–378, 1985.

[17] D. Funnemann and H. Merz, "10 eV photon detector for inverse photoemission," *Journal of Physics E: Scientific Instruments*, vol. 19, pp. 554–557, July 1986.

[18] J. Lipton-Duffin, *First results from a third generation KRIPES system.* National Library of Canada= Bibliotheque nationale du Canada, Ottawa, 2002.

[19] N. Ashcroft and N. Mermin, *Solid State Physics.* Cengage, 2021.

[20] M. P. Seah and W. Dench, "Quantitative electron spectroscopy of surfaces: A standard data base for electron inelastic mean free paths in solids," *Surface and interface analysis*, vol. 1, no. 1, pp. 2–11, 1979.

[21] J. Girard, Y. Samson, S. Gauthier, S. Roussel, and J. Klein, "Stm study of the nucleation and annealing of ion bombardment induced defects on cu (100)," *Surface science*, vol. 302, no. 1-2, pp. 73–80, 1994.

[22] M. Henzler, "Texture of surfaces cleaned by ion bombardment and annealing," *Surface Science*, vol. 22, no. 1, pp. 12–18, 1970.

[23] J. B. Pendry, "Low-energy electron diffraction," in *Interaction of Atoms and Molecules with Solid Surfaces*, pp. 201–211, Springer, 1974.

[24] F. Jona, J. Strozier Jr, and W. Yang, "Low-energy electron diffraction for surface structure analysis," *Reports on Progress in Physics*, vol. 45, no. 5, p. 527, 1982.

[25] N. G. Stoffel and P. D. Johnson, "A low-energy high-brightness electron gun for inverse photoemission," *Nuclear Instruments and Methods in Physics Research Section A: Accelerators, Spectrometers, Detectors and Associated Equipment*, vol. 234, pp. 230–234, Feb. 1985.

[26] N. Smith and D. P. Woodruff, "Inverse photoemission from metal surfaces," *Progress in surface science*, vol. 21, no. 4, pp. 295–370, 1986.

[27] S. Raj and D. D. Sarma, "Optimization of a low-energy, high brightness electron gun for inverse photoemission spectrometers," *Review of Scientific Instruments*, vol. 75, pp. 1020–1025, Apr. 2004.

[28] G. Ozur, D. Proskurovsky, V. Rotshtein, and A. Markov, "Production and application of low-energy, high-current electron beams," *Laser and Particle Beams*, vol. 21, no. 2, pp. 157–174, 2003.

[29] S. Dushman, "Thermionic emission," *Reviews of Modern Physics*, vol. 2, no. 4, p. 381, 1930.

[30] H. Yamane, H. Setoyama, S. Kera, K. Okudaira, and N. Ueno, "Low-energy electron transmission experiments on graphite," *Physical Review B*, vol. 64, no. 11, p. 113407, 2001.

[31] C. E. Sosolik, A. C. Lavery, E. B. Dahl, and B. H. Cooper, "A technique for accurate measurements of ion beam current density using a Faraday cup," *Review of Scientific Instruments*, vol. 71, pp. 3326–3330, Sept. 2000.

[32] R. H. Mattish, T. J. Burke, P. R. Johnson, C. E. Sosolik, and J. P. Marler, "Deflected beam method for absolute current density determination," *AIP Advances*, vol. 13, p. 055206, May 2023.

[33] R. Mattish, "Deconvolution of Measured Current Profiles," July 2022. https://github.com/rhmatti/Current-Density-Deconvolution.

[34] A. Zumbülte, A. B. Schmidt, and M. Donath, "Momentum resolution in inverse photoemission," *Review of Scientific Instruments*, vol. 86, p. 013908, Jan. 2015.

[35] S. Instruments, "Low energy electron sources: NEK-150," Nov. 2015. https://www.staibinstruments.com/nek-150/.

[36] G. F. Knoll, *Radiation Detection and Measurement*. John Wiley & Sons, Aug. 2010. Google-Books-ID: 4vTJ7UDel5IC.

[37] D. Sim, "English: Plot of relative level of ion-pair current with increasing voltage applied between anode and cathode for a wire cylinder ionisation detection system with constant incident ionising radiation," June 2012. https://commons.wikimedia.org/wiki/File:Detector_regions.gif.

[38] C. Thiede, I. Niehues, A. B. Schmidt, and M. Donath, "The acetone bandpass detector for inverse photoemission: operation in proportional and Geiger–Müller modes," *Measurement Science and Technology*, vol. 29, p. 065901, Apr. 2018. Publisher: IOP Publishing.

[39] Cremat Inc., "Cr-110-r2.2 charge sensitive preamplifier: application guide." https://www.cremat.com/CR-110-R2.2.pdf.

[40] Cremat Inc., "Cr-200 gaussian shaping amplifier: application guide." https://www.cremat.com/CR-200-R2.1.pdf.

[41] M. Budke, V. Renken, H. Liebl, G. Rangelov, and M. Donath, "Inverse photoemission with energy resolution better than 200mev," *Review of Scientific Instruments*, vol. 78, no. 8, 2007.

[42] F. Schedin, G. Thornton, and R. I. G. Uhrberg, "Windows and photocathodes for a high resolution solid state bandpass ultraviolet photon detector for inverse photoemission," *Review of Scientific Instruments*, vol. 68, pp. 41–46, Jan. 1997.

[43] J. A. Lipton-Duffin, A. G. Mark, and A. B. McLean, "Photon detection with n-propanol and C2H6O isomers," *Review of Scientific Instruments*, vol. 73, pp. 3149–3153, Sept. 2002.

[44] A. F. Campos, P. Duret, S. Cabaret, T. Duden, and A. Tejeda, "Spin-and angle-resolved inverse photoemission setup with spin orientation independent from electron incidence angle," *Review of Scientific Instruments*, vol. 93, no. 9, 2022.

[45] A. Tamai, W. Meevasana, P. King, C. Nicholson, A. Torre, E. Rozbicki, and F. Baumberger, "Spin-orbit splitting of the shockley surface state on cu(111)," *Physical Review B*, vol. 87, 01 2013.

[46] S. Banik, A. Shukla, and S. Barman, "Optimal operating conditions and characteristics of acetone/ caf2 detector for inverse photoemission spectroscopy," *Review of scientific instruments*, vol. 76, no. 6, 2005.

[47] E. Chulkov, I. Sarria, V. Silkin, J. Pitarke, and P. Echenique, "Lifetimes of image-potential states on copper surfaces," *Physical review letters*, vol. 80, no. 22, p. 4947, 1998.

[48] M. Maniraj, S. D'Souza, J. Nayak, A. Rai, S. Singh, B. Sekhar, and S. Barman, "High energy resolution bandpass photon detector for inverse photoemission spectroscopy," *Review of Scientific Instruments*, vol. 82, no. 9, 2011.

[49] B. Reihl, J. Gimzewski, J. Nicholls, and E. Tosatti, "Unoccupied electronic states of graphite as probed by inverse-photoemission and tunneling spectroscopy," *Physical Review B*, vol. 33, no. 8, p. 5770, 1986.

[50] I. Schäfer, M. Schlüter, and M. Skibowski, "Conduction-band structure of graphite studied by combined angle-resolved inverse photoemission and target current spectroscopy," *Physical Review B*, vol. 35, no. 14, p. 7663, 1987.

[51] N. Holzwarth, S. G. Louie, and S. Rabii, "X-ray form factors and the electronic structure of graphite," *Physical Review B*, vol. 26, no. 10, p. 5382, 1982.

[52] D. Niesner and T. Fauster, "Image-potential states and work function of graphene," *Journal of Physics: Condensed Matter*, vol. 26, no. 39, p. 393001, 2014.